The Origin of Vertical Structure in a Simulated Galactic Disk

by

Nicholas Loewen
B.Sc., University of Victoria, 2016

A Thesis Submitted in Partial Fulfillment of the
Requirements for the Degree of

MASTER OF SCIENCE

in the Department of Physics and Astronomy

The Origin of Vertical Structure in a Simulated Galactic Disk

by

Nicholas Loewen
B.Sc., University of Victoria, 2016

Supervisory Committee

Dr. J. Navarro, Supervisor
(Department of Physics and Astronomy)

Dr. J. Willis, Departmental Member
(Department of Physics and Astronomy)

Supervisory Committee

Dr. J. Navarro, Supervisor
(Department of Physics and Astronomy)

Dr. J. Willis, Departmental Member
(Department of Physics and Astronomy)

ABSTRACT

We use the Apostle simulation suite to study the formation of galactic disks, in order to better understand the origin of their vertical structure. We select a disk-dominated Milky Way analogue galaxy from the simulation which experiences a minimum of external interaction with its environment as a generalizable test case. The simulated stellar disk is found to form upside-down from a gradually thinning, flared gaseous disk, where the rate of thinning is regulated by feedback from in-situ star formation. No significant sources of vertical heating are present in the disk, allowing the vertical structure of newly-formed stellar populations to be preserved over time. As a result, the properties of the stellar disk as a function of age accurately trace the properties of the gaseous disk as a function of time. This allows us to derive a physical model, in which the disk is isothermal, in quasi-hydrostatic equilibrium, and vertically supported by bulk motions rather than thermal pressure, which relates the present-day vertical age-velocity dispersion relation (AVR) at a given radius to the local star formation history as a simple power-law relation, with a best fit power law index $n = 1.82$. This relation is then applied to the observed AVRs in the Milky Way from the recent literature, providing a predicted local star formation history for the Milky Way as a function of radius. We then compare this predicted history to others from the literature, in order to test whether our upside-down model from the simulation is consistent with the observed Galaxy. We also examine the observed ratio of vertical to radial velocity dispersions for consistency with our model. While our predicted history is broadly consistent with other predictions, the range of possible histories in the literature makes a more definitive conclusion difficult.

Contents

List of Tables

List of Figures

Acknowledgements

I would like to thank:

Ruth for being amazing

The parentals for pushing me over the last hill

Julio for being patient

Dedication

To gardening and coke floats

Chapter 1

Introduction

1.1 Preface

Galaxies are massive, gravitationally bound structures composed of stars, gas, and dark matter, and are among the most visually striking objects visible in the night sky. Recent decades have seen significant progress in our understanding of galaxy formation and evolution. This has been due in great part to large-scale surveys of both distant galaxies and stars across our own Milky Way, as well to improvements in computational power that have enabled increasingly sophisticated numerical simulations.
The study of galaxies is important not only to understand the context in which our Solar System exists, but also because the population and properties of galaxies provide important tests for cosmological models.

The content of this thesis concerns one small part of this picture - the origin of vertical structure in galactic disks. Our goal for this research is to understand how such structure arises given the current theoretical framework, and to apply this understanding to the Milky Way to better explain and understand its origins.

•

1.2 Cosmology

1.2.1 Cosmological Model

The current standard cosmological model is the Λ Cold Dark Matter model (LCDM hereafter), which is the model adopted in our simulations. It describes a flat universe in which the mass budget is dominated by a non-luminous and collision-less

dark matter component, with accelerating cosmic expansion in the current epoch. Structure in LCDM originates in the early universe from perturbations in an otherwise homogeneous matter density distribution, the power spectrum of which has been imprinted on the temperature of the Cosmic Microwave Background (CMB). These perturbations grow over time, and form a network of sheets, clusters, and connecting filaments referred to as the cosmic web.
LCDM has thus far proven very successful in explaining observations in linear regimes (where crossing times are larger than a Hubble time), through fits to the power spectrum of the CMB (eg. Komatsu et al. (2011)), distance-velocity measurements (eg. Kowalski et al. (2008)), and gravitational lensing (eg. Massey et al. (2007), Suyu et al. (2010)).

The study of LCDM in non-linear regimes (where crossing times are on the order of or less than a Hubble time) can be done mainly through N-body simulations (eg. Millennium (Springel et al., 2006)), which have been essential tools for studying systems that are too complex for analytical approaches. Simulations with this cosmology have been similarly successful in understanding observed large-scale structure (eg. Tegmark et al. (2006)) and the properties of galaxy clusters (eg. Vikhlinin et al. (2009)).

1.2.2 Halos in LCDM

The good agreement between LCDM and observations on these larger scales enables cosmological simulations to be used predictively for structure on smaller (ie. galactic) scales. In these regimes, dark matter in LCDM forms triaxial structures that can be characterized with universal density profiles (Navarro et al., 1997). These are referred to as dark matter halos.
Halos cluster and merge over time, such that in the present-day each is the product of a history of hierarchical assembly of many smaller constituent halos (White & Rees, 1978)(White & Frenk, 1991). Combined with the initial distribution of overdensity perturbations, the resulting distribution of halos is well matched by observed galaxy distributions from redshift surveys (eg. 2dFGRS (Colless et al., 2003), SDSS (Tegmark et al., 2004), 2MASS (Huchra et al., 2005)).
This, along with their deep potential wells and short crossing times, means that dark

matter halos (or at least those with masses around $10^8 - 10^{12}\,M_\odot$) are expected to be the sites of galaxy formation.

1.3 Galaxies

1.3.1 Baryons

On cosmological scales (eg. $\gtrsim 1Mpc$) luminous baryonic matter (gas and stars) traces the same overall structure as the gravitationally dominant dark matter, and what we call galaxies are baryonic structures bound within dark matter halos.
However, modelling the physics of baryons is considerably more difficult than that of the exclusively gravitational dark matter. The added physics - such as pressure, radiative cooling, multi-phase gas, and the formation of compact objects like stars and black holes - significantly expands the range of spatial scales involved. Properly simulating this entire range is beyond current computational capabilities, so the effects sub-resolution physics have on larger scales must be approximated (see Somerville & Davé (2015) for a detailed review).
These additional complications mean that, although the cosmological context is fairly well-established, many aspects of galaxy formation and evolution are still not well understood.

Despite this, it is clear that the inclusion of these physical processes is necessary to properly model galaxies. Particularly important is feedback: energy injected into the intergalactic medium (IGM) and interstellar medium (ISM) by active galactic nuclei and ejecta from supernovae. N-body simulations of galaxy formation have found that, unhindered, gas cools and collapses far too quickly, causing unrealistically massive galaxies to form, and most of the gas is consumed by star formation too early (White & Rees, 1978)(White & Frenk, 1991)(Katz, 1992)(Benson et al., 2003). Feedback counterbalances the cooling process through the injection of energy back into the galactic gas component, allowing it to collapse more slowly. This also regulates the star formation rate so that more gas is available to form stars at later cosmic times.

The inclusion of reasonable feedback prescriptions is necessary to match observed galactic sizes, angular momenta, and rotation curves (eg. Sales et al. (2010)), as well as reconcile the observed galaxy mass function with that of the predicted halo mass function in LCDM, especially at lower masses.

Though different implementations for feedback can produce some variation (Scannapieco et al., 2012), all have the overall effect of re-injecting energy to hinder collapse, and it is now possible to examine detailed elements of galaxy formation with hydrodynamical simulations (eg. Illustris (Vogelsberger et al., 2014), EAGLE (Schaye et al., 2015), NIHAO (Wang et al., 2015)), Auriga (Grand et al., 2017) etc.).

1.3.2 General Morphology

Galaxies appear to have two main morphological components: a spheroid and a planar disk. The degree to which these components dominate is broadly correlated with the bimodal galaxy colour distribution, where blue (star-forming) galaxies tend to be disk-dominated and red (non star-forming) galaxies tend to be spheroid-dominated (Strateva et al., 2001).
This is generally consistent with a scenario in which the primary driver behind the current morphology of a galaxy is its merger and mass accretion history due to hierarchical assembly. Spheroidal components are generally produced by the disruption and mixing of pre-existing stellar populations by mergers, while disk components result from the smooth collapse of gas into a plane in which stars are able to form. In the absence of major mergers the disk component is preserved over time.

Though the origin of spheroidal components of a galaxy are of interest, in this work we focus exclusively on properties of galactic *disks*.

1.4 Galactic Disks

1.4.1 General Formation Scenario

Gaseous disks form via the dissipation of energy while conserving angular momentum, resulting in a gradual collapse into a rotationally supported plane. This gas can originate both from mergers between gas-rich halos or from accretion flows from the surrounding environment, and sustained gas inflow can feed galactic disks well past initial formation.
Specifically, it is the ability of gas to lose kinetic energy via radiative cooling, unlike dark matter or populations of stars, that enables the formation of a disk. Thus, a galaxy that has a disk component must first have had (or still have) the gas available from which to form it.

The stellar disk component originates from in-situ star formation in the gaseous disk. These stars inherit the chemical composition and kinematics of the gas from which they formed, such that the properties of a stellar disk reflect the cumulative properties of the gaseous disk over time. In this way, stars can provide insight into the conditions of the gas at the time of their formation.

1.4.2 Radial Structure Formation

The radial structure of a gaseous disk can be generally described by an exponential mass surface density profile, with a radial scale length dependent on a combination of the total angular momentum of the gas and the shape of the galactic gravitational potential (Mo et al., 1998)(Fall & Efstathiou, 1980). The inner regions of the disk are denser - this is due not only to the deeper local potential, but also because of the nature of accreted gas over time. In a hierarchically clustering universe, we expect that gas with higher angular momentum relative to a galactic potential will fall in at later times, and settle at larger radii (Benson, 2010). The lower angular momentum gas is accreted earlier and finds itself deposited at comparatively smaller radii.
In this scenario a galaxy is said to form 'inside-out', as the relative magnitude of star formation gradually moves outwards. This behaviour has also been seen in N-body simulations (eg. Bird et al. (2013)) and is the assumed mode of gas infall in many galactic evolution models (eg. Chiappini et al. (1997), Vera-Ciro et al. (2016), Kawata et al. (2017), Frankel et al. (2018)). The resulting stellar disk will inherit both a negative radial metallicity gradient (where inner regions are more metal-rich) as well as a positive radial age gradient (where inner regions are on average older than outer regions).

1.4.3 Radial Migration

If stars did not move from their birth radii we would expect little change in the radial properties of co-eval stars over time, and stellar properties by age would precisely trace the properties of the gas from which they formed. Assuming the local ISM was chemically homogeneous (which seems to be the case in the solar neighbourhood (Przybilla et al., 2008)), this would result in tight correlations between age and chemical abundances at a given radius. This is not, however, what is observed in the

Milky Way: there is considerable scatter in the local age-metallicity relation (AMR) (eg. (Edvardsson et al., 1993)(Haywood et al., 2013)(Bergemann et al., 2014)). Some scatter is expected given the epicyclic nature of galactic orbits, in which circular orbits oscillate radially while conserving angular momentum (see (Binney & Tremaine, 1987)), but constraints on this effect based on the local radial velocity dispersion renders it insufficient to explain observations.

Resolving this discrepancy requires a mechanism by which the orbital angular momenta of stars can be changed while keeping their orbits circular. This can be accomplished via corotation resonance with a transient non-axisymmetric overdensity in the disk such as spiral arms (Sellwood & Binney, 2002)(Minchev & Famaey, 2010) or a galactic bar (Brunetti et al., 2011). Including such a mechanism provides the necessary scatter in the AMR to match observations (Sellwood & Binney, 2002)(Schönrich & Binney, 2009). We refer to this mechanism (in which orbital angular momentum is changed) as churning, and other mechanisms such as epicyclic motions (which conserve angular momentum) as blurring.

There is reasonable consensus in the literature on the effects of migration on the *radial* properties of a galactic disk. Besides increasing the scatter in the local age-metallicity relation, the most obvious effect of migration is the flattening of radial metallicity gradients, as comparatively metal-rich stars from inner regions migrate outwards and vice-versa for outer regions (though noticeable flattening requires significant migration (Grand et al., 2015)). Furthermore, metallicity distribution functions obtain a distinct 'skewness' as a function of radius, where at inner radii the distributions have an extended lower metallicity wing due to migrators being from primarily further out (Hayden et al., 2015)(Loebman et al., 2016). Similarly, distributions at outer radii have extended high metallicity wings.

1.4.4 External Interactions

External interactions of varying magnitude can occur throughout a galaxy's history, and can impact both the formation and evolution of its disk. Satellite interactions have been found to be capable of driving radial migration not unlike internal overdensities (Villalobos & Helmi, 2008)(Bird et al., 2012), and mergers in the plane of the

disk can dynamically heat up existing stellar populations (eg. (Helmi et al., 2018)) or deposit stars formed ex-situ. Even without disturbing pre-existing stars, local accretion of pristine gas can change the kinematic and chemical patterns of formation in the disk.

Furthermore, a major merger can completely disrupt an existing disk, resulting in a change in the dominant morphology of a galaxy from disk to spheroid. Subsequent accretion of additional gas can re-enable disk formation, such that galaxies can form and lose and reform disks according to their individual merger histories (Steinmetz & Navarro, 2002), but little trace of a pre-existing disk would persist.

Such events are dependent on the individual history and environment of a galaxy, and thus are difficult to generalize. For simplicity we will choose to focus on time periods in our simulated disks which are relatively quiescent (ie. environmentally isolated) in order to keep our results as general as possible.

1.5 Vertical Disk Structure

1.5.1 Formation

The vertical structure of a purely gaseous disk is expected to be in a state of equilibrium between a restoring pressure and the compressive force of the gravitational potential. This can be further modelled analytically with simple assumptions, such as a razor-thin disk approximation, the state of the gas (eg. isothermal), or the relative importance of the gravity of the dark matter halo compared to the self-gravity of the baryonic disk (this will be explored in detail in Chapter 3).

Unsurprisingly, however, including star formation in this gaseous disk makes this picture more complex. First is the effect of the relative timescales of vertical cooling and star formation on the stellar populations over time. If star formation timescales are smaller than cooling timescales, successive stellar populations would form at progressively shorter scale heights (referred to as 'upside down' formation (Bird et al., 2013)(Grand et al., 2017)), resulting in a clear dependence on final vertical structure with stellar age. This would also naturally produce vertical metallicity gradients with increasing metallicity at smaller heights, as the gas gradually enriches as the disk thins. In the opposite case stars would form with similar vertical scale heights over time and there would be little difference kinematically between successive age cohorts.

Furthermore, the full extent of the effects of stellar feedback on vertical structure

are not still well understood. Though the existing prescriptions used in simulations succeed in reproducing the radial properties of disks, vertically they tend to be too thick (see eg. Trayford et al. (2017),Benítez-Llambay et al. (2018)).

1.5.2 Vertical Evolution from Migration

While the radial effects of stellar migration introduced above are reasonably well understood, the extent of the effects of migration on the *vertical* structure of the disk are not. Under the assumption that stars preserve their vertical actions when they migrate radially, we would expect that stars migrating outwards (inwards) would find themselves in a less (more) dense disk environment with a weaker (stronger) restoring force, and thus end up deposited at larger (smaller) heights above the disk (see Minchev (2016) and references therein). While this does not appear to affect the overall thickness of the disk, since the changes at a given radius due to inward migrators would be balanced by outward migrators, it would induce disk flaring (an increase in scale height with radius) at the extreme ends. This picture is somewhat complicated by results from Vera-Ciro et al. (2014) who find that most migrators are stars close to the plane of the disk with small vertical excursions ('provenance bias'), which would depress migration-induced flaring in the outer disk.
Since migrators generally inherit the kinematic properties of their new radii, it is in the chemical signatures of these processes where we must look to disentangle them. However, the exact role of migration in producing the observed chemical substructure (eg. vertical metallicity gradients) in the Milky Way has so far remained unclear (Schlesinger et al., 2014)(Hayden et al., 2014)(Bovy et al., 2016). While models that invoke migration can succeed in explaining what is observed, they depend on assumptions of the initial structure from formation, and different initial conditions can significantly change the end result under migration (Kawata et al., 2017). Others find that migration cannot fully explain what is observed based on kinematic limitations (Vera-Ciro et al., 2016) or that similar results can be obtained without the need for migration at all (Ciucă et al. (2018), and Navarro et al. (2018) which includes work by the authour of this thesis).

1.5.3 Vertical Heating

Changes in stellar disk structure are also driven by other sources of heating. Stars in the plane of the disk are expected to scatter off disk substructures (bars and spiral arms) and local overdensities such as giant molecular clouds (GMCs) (Lacey, 1984). While the former primarily heats stars in the plane of the disk, the latter may act to convert the orbital in-plane motion of a star into *vertical* motion out of the plane of the disk, such that a population of stars scattering in this way will exhibit increasing vertical velocity dispersions and scale heights over time. Assuming that a disk were to initially form with a constant thickness at all times, such scattering would produce both a positive vertical age-velocity dispersion relation (AVR), as well as a negative vertical metallicity gradient, that is qualitatively similar to what you would expect from upside down disk formation. Such a relation is observed in the Milky Way (eg. Casagrande et al. (2011),Sanders & Das (2018)), but its origins are still not entirely clear.

Since GMCs are one of the few sources of vertical heating, and spirals primarily heat stars in the plane, the ratio of the vertical to radial velocity dispersions (σ_z/σ_R) of a stellar population is a useful measure of the relative importance of these two processes. A greater contribution from spiral arm heating noticeably decreases this ratio (Jenkins & Binney, 1990), such that in a scenario where star formation rates in the disk (and thus density of GMCs) drop as the disk mass grows, we would expect that older populations of stars should have a larger ratio than younger stars (Aumer et al., 2016b). Recent observations suggest that this may be occurring in the Milky Way, but the trends with age and radius are complex and require further modelling (Mackereth et al., 2019).

1.6 Motivation

The goal of this work is to explore the origin of vertical disk structure of simulated disks in order to better understand what is observed in the Milky Way.

We use Apostle (A Project Of Simulating The Local Environment)(Fattahi et al., 2016), which is a set of 12 cosmological zoom-in hydrodynamical simulations of local-group analogues (ie. the Milky Way, M31, and their surroundings). These produce 24 total primary galaxies with approximately MW mass, of which a number are disk-dominated.

Our earlier work on Milky Way-analogue disks in APOSTLE (Navarro et al. (2018), N18 hereafter) found that they form upside-down and experience little significant change over time from either radial migration or secular vertical heating. Radial and vertical metallicity gradients as well as the flaring of mono-abundance populations, which showed qualitative similarities to the Milky Way, were produced exclusively from formation rather than from evolution.
We now focus specifically on vertical kinematic structure at a given radius, namely the AVR, to expand on what was presented in N18.

Stars in the Milky Way's solar neighbourhood show increasing vertical velocity dispersion with age (Holmberg et al., 2007)(Casagrande et al., 2011), and recent large-scale stellar surveys indicate that this is also the case over a large range of galactic radius (Sanders & Das, 2018)(Mackereth et al., 2019). While upside-down formation is a plausible explanation, and is how most cosmological simulations produce this signature, recent work by Ting & Rix (2018) has shown that heating from GMC scattering is sufficient to fully reproduce the observed AVR even when starting from an initially constant birth temperature. Heating therefore cannot currently be ruled out as a significant (or sole) contributor to the Milky Way's vertical disk structure, and the relative importance of formation versus heating is uncertain.
Our simulations do not resolve GMC scattering, enabling us to more easily isolate the signatures of formation mechanisms on the final structure of galactic disks. By constructing a simple model based on the physical processes driving our simulation's vertical structure, which we can then test against observations and models of the Milky Way, we can constrain the contribution of upside-down disk formation to setting the Milky Way's vertical disk structure.

In this thesis we will first describe the simulations and characterize the global properties and individual formation histories of the disks it produced (Chapter 2). We will then explore in depth the origin of the simulated disk's vertical structure over time and construct a simple predictive model (Chapter 3). This model will then be applied to observations of the vertical properties of the Milky Way's stellar disk, and the results compared to the literature (Chapter 4).

Chapter 2

Simulations

In this chapter we introduce the simulations used in our work, characterize the disk galaxies they produce, and select one where the disk formed quiescently for detailed analysis.

2.1 Overview

We use disks produced in the APOSTLE (A Project Of Simulating The Local Environment) simulation suite in this work (Fattahi et al., 2016). It is an N-body cosmological hydrodynamic simulation (ie. including both dark matter and baryons) comprised of a series of 12 zoom-in re-simulations of Local Group-like regions from a larger dark matter only cosmological volume.
The aim of APOSTLE is to provide a test bed for the predictions of LCDM cosmology on smaller scales, for which observations are limited to the Local Group. The simulation has proven very successful in reproducing observed properties of Local Group satellites, and in resolving challenges to LCDM on these scales through the effects of baryonic processes (Sawala et al., 2016).

2.1.1 Volume Selection

Zoom-in regions were selected based on their Local-Group-like (LG) environments and kinematics at z=0, with criteria as follows: two Milky Way and M31 analogue DM halos with total combined virial mass in the range $[10^{12.2}, 10^{12.6}]$ $M_\odot$, separation in the range [600, 1000] kpc, relative radial velocity in the range $[-250, 0]$ $km\,s^{-1}$, relative tangential velocity less than $100\,km\,s^{-1}$, and recession velocities of outer group members between [120, 290] $km\,s^{-1}$ at 2.5 Mpc with velocity-distance slopes between

[70, 140] $\mathrm{km\,s^{-1}\,Mpc^{-1}}$.

As a result, the simulation provides a set of 24 (two for each of 12 volumes) primary galaxies with masses and environments comparable to the Milky Way. This enables the study of galactic disk formation and evolution for Milky Way analogues with initial conditions and environments arising naturally rather than being chosen ad hoc.

2.1.2 Halo Identification

Halos and the particles associated with them are identified using a friends-of-friends (FOF) algorithm (Davis et al., 1985). Self-bound substructures within each halo (subhalos, such as may contain a satellite galaxy) are further identified with the SUBFIND algorithm (Springel et al., 2001).

Each halo is characterized by its virial properties, which in the simulation are defined based on the value of the critical density of the universe: the virial radius R_{200} is the radius of a sphere in which the enclosed mean density is equal to 200 times the critical density, and the virial mass M_{200} is the total mass enclosed within R_{200}. We further define a *galactic* radius $r_{gal} \equiv 0.15 \times R_{200}$. This is done to select the volume which encompasses the baryonic galaxy embedded within each dark matter halo, and at z=0 is typically on the order of 30 kpc for the primaries.

2.1.3 Cosmological Parameters and Resolution

APOSTLE uses the N-body Tree-PM smoothed particle hydrodynamics (SPH) code GADGET3 (Springel, 2005), with subgrid physics based on the EAGLE simulations (Schaye et al., 2015). The simulation assumes an LCDM cosmology with parameters from WMAP7 (Komatsu et al., 2011) (shown in Table 2.1). The simulation has three different resolution runs (HR, MR, LR); we use only the medium resolution (MR) in our analysis, as it is the highest resolution which includes all volumes at the time of writing (not all have yet been run in the highest resolution). Particle mass resolutions and softenings for each volume in MR are shown in Table 2.2, along with virial masses of the primary galaxies, separations, and velocities on which the volume selections were based.

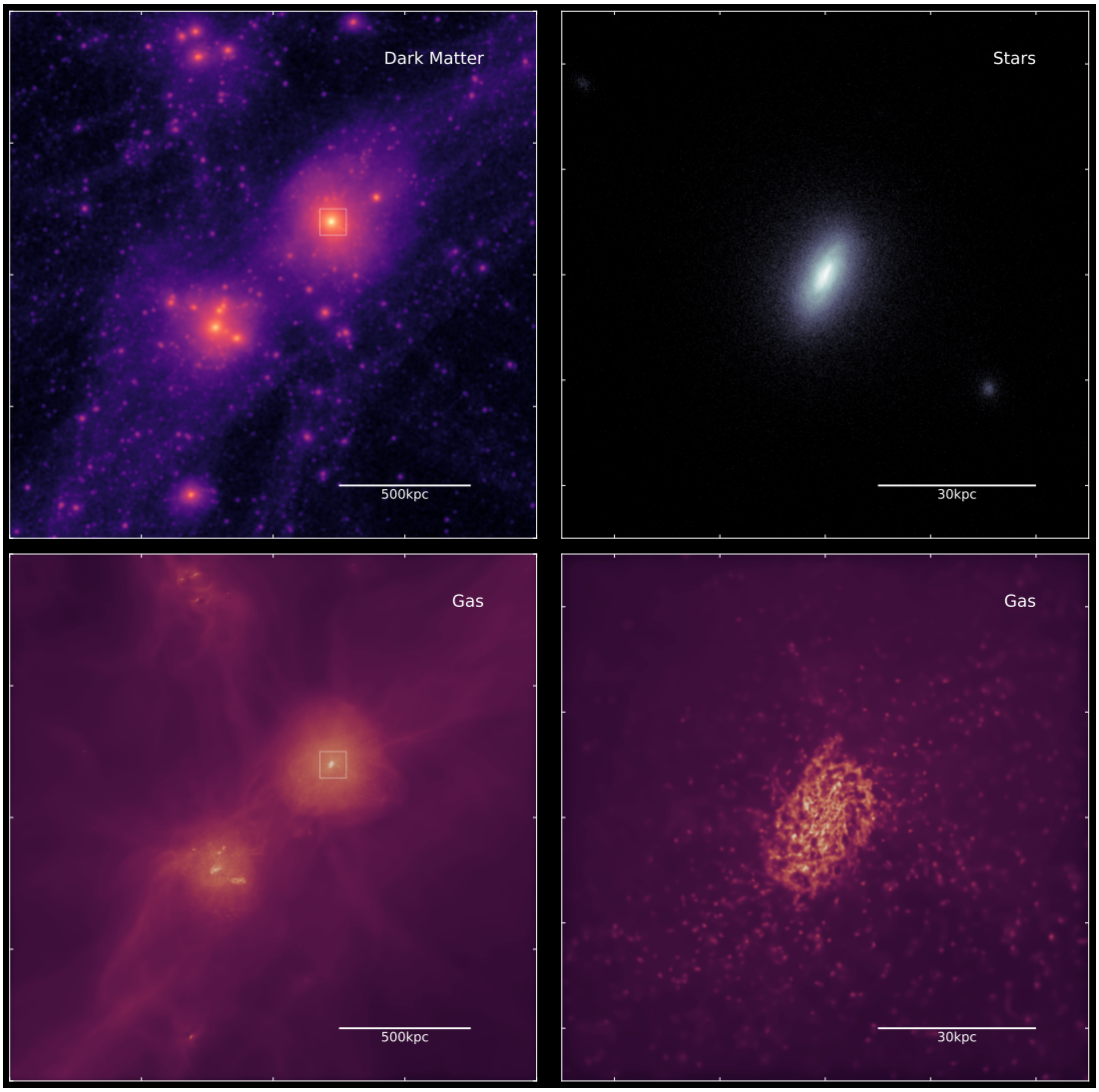

Figure 2.1: Visualization of APOSTLE Volume 1. Top left shows dark matter density, where the two primary halos are clearly visible. Bottom left is the same but for gas density. Top right is the stellar density of the upper right galaxy (V1G0), and bottom right is the same but again for gas density.

parameter	value
Ω_m	0.272
Ω_Λ	0.728
Ω_b	0.0455
h	0.704
σ_8	0.81
n_s	0.967

Table 2.1: Cosmological parameters from WMAP7 (Komatsu et al., 2011) used in APOSTLE, where Ω_m, Ω_Λ, and Ω_b are average densities of matter, dark energy, and baryonic matter in units of the critical density for closure, h is the hubble parameter, σ_8 is the square root of the linear variance of the matter distribution in spheres of radius $8\,h^{-1}$ Mpc, and n_s is the power-law index of the power spectrum of primordial adiabatic perturbations.

2.1.4 Gravity and Hydro Solvers

Gravitational forces are calculated using a hybrid Tree-PM method, which uses a potential mesh (PM) calculation for distant forces and a tree method for smaller scales. This combines the advantages of PM (faster computational time and easily implemented periodic forces) with the adaptive resolution of tree methods to maximize the dynamic range in the simulation. The net gravitational force is calculated at every timestep for each individual particle of every type (ie. stars, gas, dark matter) using a Plummer gravitational softening.

Gas hydrodynamics is simulated using Smoothed Particle Hydrodynamics (SPH), a Lagrangian method which uses discrete particles to measure the continuous properties of a fluid (see Monaghan (1992) and Springel (2010a) for reviews on SPH methods). To briefly summarize, fluid properties are measured using a kernel interpolation, in which the properties of a particle (eg. density, pressure, temperature) contributes to other nearby particles based on a distance-dependent kernel function, and mass is tracked directly by the movement of individual particles. Fluid pressure is included alongside gravity when computing acceleration of the gas particles at each timestep.

GADGET3 uses the pressure-entropy SPH formulation from Hopkins (2013), which improves the handling of shocks and surface instabilities compared to classic SPH

Volume	M^0_{200} $[10^{12} M_\odot]$	M^1_{200} $[10^{12} M_\odot]$	**Separation** $[kpc]$	V_r $[km/s]$	V_t $[km/s]$	m_{gas} $[10^5 M_\odot]$	ϵ_{max} $[pc]$
1	1.66	1.10	850	-51	35	1.20	307
2	0.85	0.83	809	-39	97	1.25	307
3	1.52	1.22	920	-35	84	1.25	307
4	1.38	1.35	790	-59	24	1.22	307
5	0.93	0.87	828	-33	101	1.25	307
6	2.36	1.21	950	-18	60	1.27	307
7	1.88	1.09	664	-174	24	1.13	307
8	1.72	0.65	817	-120	96	1.10	307
9	0.96	0.68	814	-28	48	1.09	307
10	1.46	0.87	721	-63	48	1.10	307
11	0.99	0.80	770	-124	22	1.11	307
12	1.11	0.58	635	-53	50	1.09	307

Table 2.2: Virial masses of each primary at z=0, their separation, relative radial and tangential velocities, initial gas particle mass resolution, and softening lengths for MR. Dark matter mass resolutions are $m_{DM} = (\frac{1}{f_{bar}} - 1) m_{gas}$ where $f_{bar} = \Omega_b / \Omega_m$ is the universal baryon fraction.

schemes. While differences in performance remain between these modern Lagrangian approaches and Eulerian adaptive mesh methods (Springel, 2010b) they generally yield similar results in basic tests of galaxy formation - greater variation arises from in an individual simulation's prescriptions for subgrid physics (Somerville & Davé, 2015).

2.1.5 Subgrid Physics

Despite the large dynamical range achievable by modern codes, crucial physical processes remain unresolved. These must be included separately from gravity and hydro solvers to approximate the effects of the unresolved physics on the larger scales of the simulation. Details on all implemented subgrid processes can be found in Schaye et al. (2015) (and Crain et al. (2015) for calibration), but we will describe here those most relevant to this thesis - star formation and stellar feedback.

Each gas 'particle' in the simulation has an associated star formation rate. This rate is based on the observed Kennicutt-Schmidt (KS) relation (Kennicutt, 1998) which relates the surface density of star formation to the surface density of gas, but

is rewritten in terms of pressure rather than density (see Schaye et al. (2015) eq(1)). This requires an assumption on the equation of state of the gas, which in the case of EAGLE (and thus also APOSTLE) is assumed to be polytropic with ratio of specific heats $\gamma = 4/3$, but also removes the requirement for fine tuning of the parameters of star formation since the inputs are given by the parameters of the empirically observed KS relation.

This star formation rate is applied stochastically, such that in a given simulation timestep Δt, the probability of forming a star is $\min(\dot{m}_* \Delta t / m_{gas}, 1)$ where $\dot{m}_*$ is the star formation rate and m_{gas} is the mass of the gas particle. Once this condition is met, a star particle replaces the gas particle and inherits its mass, kinematics, and chemistry.

An additional restriction is placed on star formation to account for the fact that the simulations do not resolve a cold gas phase. A metallicity dependent density threshold is applied, below which the star formation rate of a gas particle is necessarily zero. The threshold is expressed in terms of a hydrogen number density $n_H = 0.1 \mathrm{cm}^{-3} (\frac{\mathrm{Z}}{0.002})^{-0.64}$, where Z is the metallicity of the gas particle (such that the threshold decreases at higher metallicities).

Stellar feedback is the combined effect of stellar winds, radiation, and supernovae from primarily massive short-lived stars. This injects energy and momentum (as well as enriched material) back into the ISM. In APOSTLE (and EAGLE) this is accomplished by adding thermal energy to surrounding gas particles after a star particle is formed. This too is applied stochastically, rather than evenly to every gas particle, so that the energy from feedback is not excessively diluted by being spread out over too much surrounding mass. This allows the injected thermal energy to be more efficiently converted to kinetic energy, and thus properly drive galactic winds and outflows (see Dalla Vecchia & Schaye (2012)).

The feedback effect is applied once per star particle 3×10^7 years after formation (the maximum expected lifetime of stars that end in core-collapse supernovae). This is shorter by $\sim$2 orders of magnitude than a typical snapshot time interval in our lower redshift simulation data, and so in our analysis it can be considered effectively instant. Stellar mass loss is applied over each time step assuming a Chabrier IMF, and the lost mass is added to surrounding gas particles. Chemical enrichment yields are also applied to the gas at the same time.

2.2 Identifying Disks in Apostle Primary Galaxies

2.2.1 Defining the Disk Component

Note that the LG-like regions of the simulation were not selected based on any criteria for the primary galaxy pair's morphological similarities to the Milky Way and M31 (ie. they were not selected to be disks). The resulting morphologies are varied, and while most have a disk component they are not necessarily disk dominated. This requires us to characterize the primaries' disks to select the best candidate(s) to study disk formation and evolution. We emphasize here that any resulting disk is *not* a direct model of either the Milky Way or of M31, as the only properties they have been selected for are similar total mass and environment. Rather, we aim to understand generalised formation and evolution scenarios, which can then be applied to other observed systems.

We first isolate each of the 24 primary galaxies from their surrounding halo and satellites by making a spherical cut to select only those particles within r_{gal}. All subsequent analyses of galaxy properties are made with this cut.
We define galacto-centric coordinates for each galaxy based on the angular momentum on the inner 30% by mass of the galaxy's star-forming gas. Star-forming gas is selected simply as those gas particles with a non-zero star formation rate (ie. above the metallicity-dependent density threshold). We find that in general this orientation has the best success in aligning the disk component of our galaxies at any given time, which is expected given the role of gas in forming the disk in the first place.

With our galaxies aligned to their disk components, we now want to characterize the degree to which that disk is morphologically dominant.
We define the circularity ϵ_j of a particle as:

$$\epsilon_j \equiv j_z/j_c \tag{2.1}$$

where j_z is the z-component of the specific angular momentum of the particle about the center of galactic potential, and j_c is what the z-component would be if a particle with the same total energy (kinetic + potential) were on a perfectly circular orbit in the plane of the disk. Thus, a particle on such an orbit would by definition have $\epsilon_j = 1$ and a collection of many such particles forming a distribution about

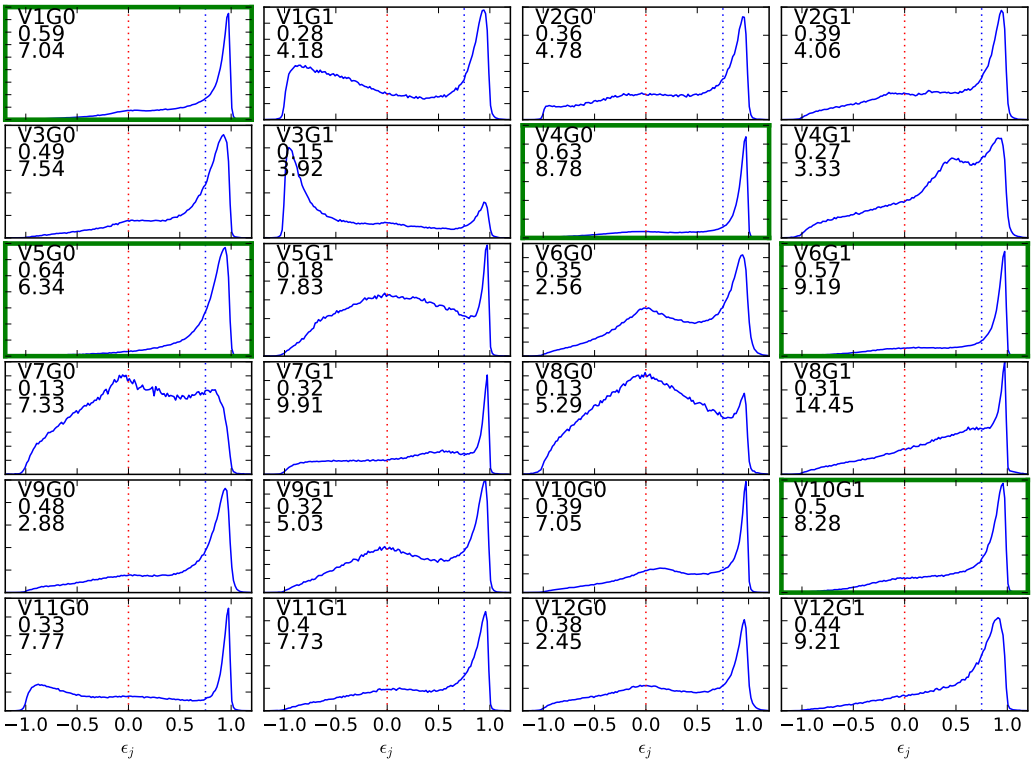

Figure 2.2: Normalized distributions of circularities ϵ_j of star particles for each of the 24 APOSTLE primaries at z=0. Galaxy IDs are shown in each panel (eg. V1G0). Spheroidal components are distributed symmetrically about $\epsilon_j = 0$ (dotted red line), while co-rotating disk components are peaks about $\epsilon_j = 1$. The numbers in the upper left of each panel are the galaxy ID, the mass fraction of the disk component (defined as being the mass fraction with $\epsilon_j > 0.75$ (dotted blue line)), and the cylindrical half-mass radius of that disk component R_h in kpc. Disk-dominated primaries (disk mass fraction above 0.5) are highlighted in green.

$\epsilon_j = 1$ would constitute a galactic disk. In contrast, spheroidal components like stellar halos or bulges form a more extended distribution about $\epsilon_j = 0$. We show the z=0 circularity distributions of the stars for each primary galaxy in Fig 2.2.

Immediately apparent is the variety in the circularity distributions. While almost all of the galaxies have a disk component (with the possible exception of V7G0), some are clearly spheroid-dominated (V5G1, V7G0, V8G0) or at least have significant spheroidal components (eg. V6G0, V9G1). There are also a few cases with asymmetric spheroidal components (V4G1, mildly V7G1, V8G1). Three galaxies have a noticeable counter-rotating disk component, as indicated by peaks about $\epsilon_j = -1$

(V1G1, V3G1, V11G0). Preliminary investigation concluded that these seem to form in-situ, originating from the accretion of gas in the plane of - but against the direction of rotation of - an existing stellar disk.
Since we wish to study a more typical or general disk formation scenario these are not ideal candidates.

We define a disk mass fraction f_{disk} as the number fraction of stars above $\epsilon_j > 0.75$ and the half-mass radius of those stars R_h. These values are indicated on the panel for each galaxy in Fig 2.2 (see caption). Our ideal cases for study are those with high disk fractions and of similar radial size to the Milky-Way.
Five galaxies have disk fractions $f_{disk} > 0.5$ (highlighted in Fig 2.2). We select these as our 'disk-dominated' galaxies, as it excludes the undesirable cases described above while maximizing the mass of the disk.

2.2.2 Quantifying Disks

For further context we show the rotation curves, total stellar masses vs R_h, and rotation speed at R_h of the primaries in Fig 2.3 with the individual disk-dominated galaxies highlighted.
Half mass radii range from $\sim$ 6 to $\sim$ 9 kpc, which are generally larger but still reasonable when compared to the $R_h \sim 6$ kpc for the Milky Way's thin disk (Bovy et al., 2012). Stellar masses range between $\sim 1-5\times10^{10} M_\odot$, which again is reasonable when compared to recent estimates of the Milky Way's total stellar mass of $\sim 5 \times 10^{10} M_\odot$ (Cautun et al., 2020).
Overall, none of the five disk-dominated galaxies have unusual properties given their stellar masses.

2.3 Assembly Histories

We now examine the mass assembly histories of the disk galaxies in order to select one for a case study. Ideally, such a galaxy would have as long a time as possible in which the disk is forming with a minimum of external influence. A scenario in which the galaxy is isolated while the disk forms and evolves gives us the best picture of innate disk formation and evolution, both chemically and kinematically.

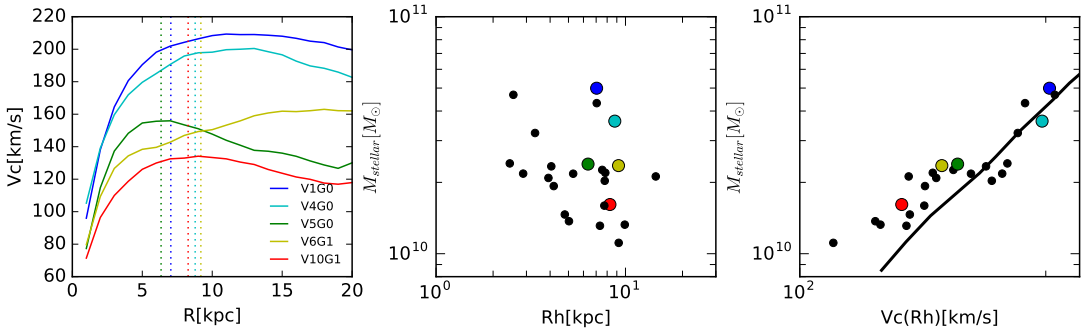

Figure 2.3: Rotation curves, total stellar masses, half-mass radii, and rotational velocity at half-mass radius for each of the disk dominated galaxies (see legend in left panel). Dotted vertical lines on left panel indicate the half-mass radius of each galaxy. Black points in middle and right panels are the other 19 primary galaxies in Apostle. Solid line in right panel is the Tully-Fisher relation for Eagle galaxies from Ferrero et al. (2017)

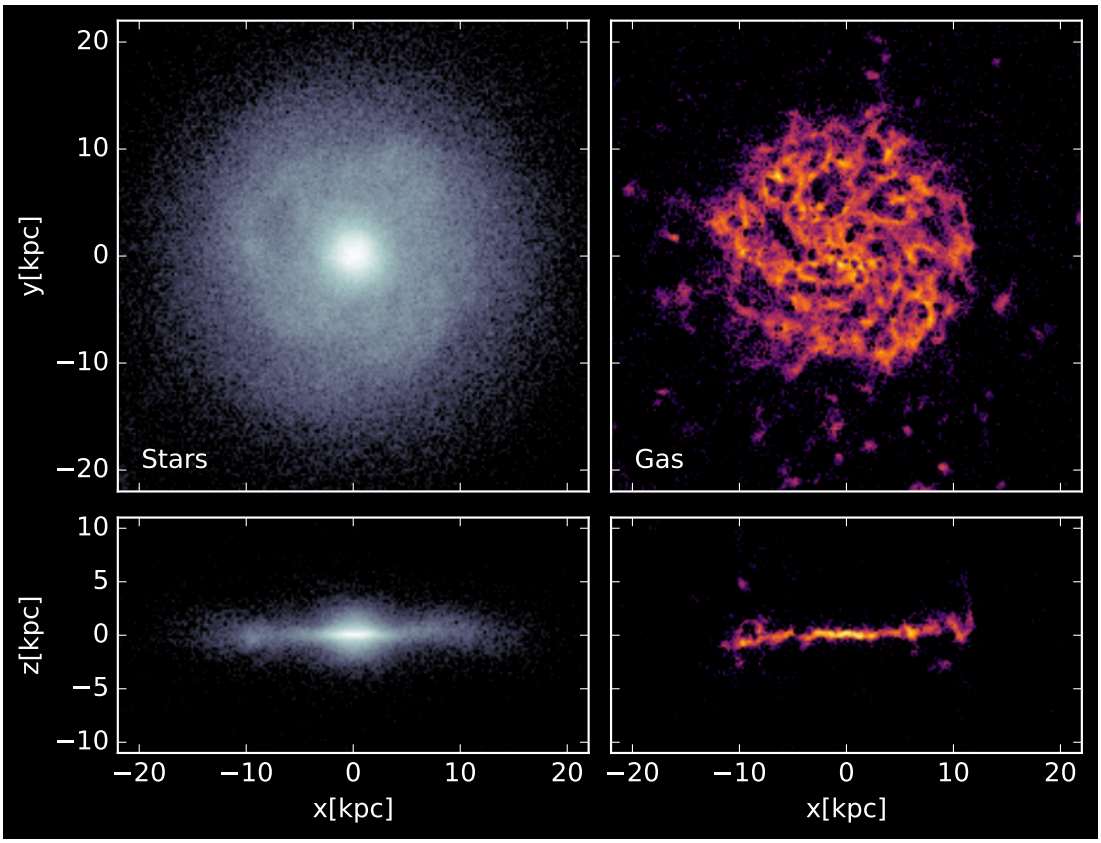

Figure 2.4: Face-on and edge-on projections of star and gas mass density for V4G0 at the end of the simulation (t_0). The edge-on panels are for a ±1kpc slice about y=0.

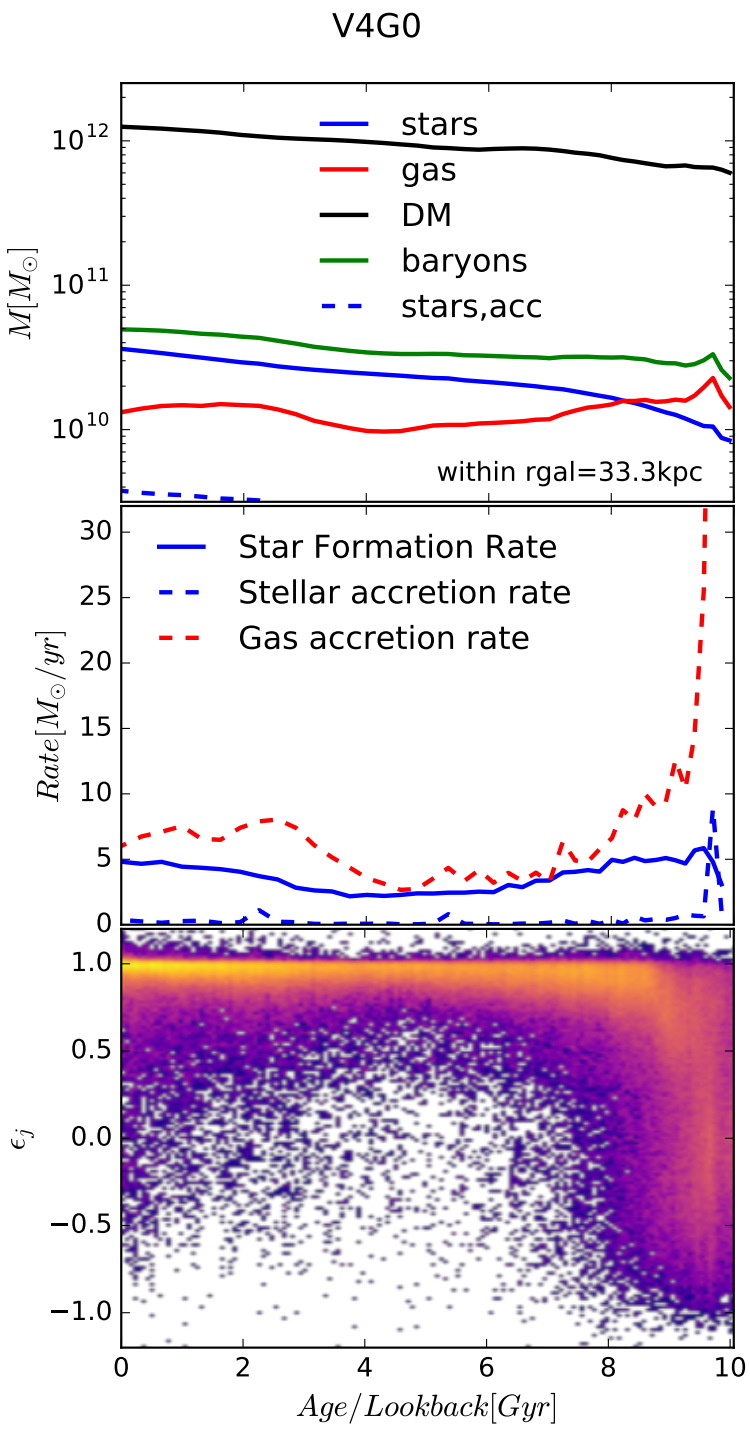

Figure 2.5: Galaxy properties over time and age for V4G0, as measured within r_{gal}. The top two panels show galaxy mass and accretion rates per component (dark matter, stars, and gas) as a function of lookback time t_{lb} ($t_{lb} = 0$ is the end of the simulation). The bottom panel shows the circularity ϵ_j as a function of stellar age at the end of the simulation.

We show one of our disk galaxies, V4G0, in Fig 2.4, as well as its global properties over time in Fig 2.5 (the same figure for the other four galaxies can be found in Appendix A.1). V4G0 will be our chosen galaxy for study, for reasons described below. We will examine its properties in detail first, and comment on the the properties of the other disk galaxies afterwards in comparison.

The circularity distributions of the disk and spheroid components are clearly correlated with stellar age, where the onset of disk formation begins at around 8 Gyrs lookback time. This is reflected in both the total masses and, especially, accretion rates over time: at greater lookback times the accretion rates are high and masses increase more steeply with time, and both are punctuated by spikes corresponding to an accretion event.
At $t_{lb} < 8$ Gyr a comparatively quiescent period begins, as accretion rates drop to a minimum and the total baryon mass becomes relatively constant, though stellar mass continues to increase as available gas is converted to stars. The circularities of stars at this age are close to $\epsilon_j = 1$. This quiescent period ends around 4 Gyrs lookback, where the gas accretion rate increases significantly.

Fig 2.6 shows total masses, accretion rates, and the age-metallicity distribution in a cylindrical section about the half-mass radius, to show the local properties within the disk in addition to the global properties of Fig 2.5. Here we see the same mass and accretion trends with time as in the global picture, but we can additionally see that the onset of gas accretion at 4 Gyrs significantly dilutes the local metallicity distributions. The overall trend of metallicity with time after 4 Gyrs *decreases*, in stark contrast to the monotonic enrichment that characterized the disk since it began to form.
This indicates that the ideal time to study disk formation for V4G0 is between 8 and 4 Gyrs lookback, before the disk is subject to a further major accretion event.

None of the other galaxies selected in the previous section have such an ideal window for disk study, as their disk formation periods are either noticeably less isolated (eg. V6G1) or have similar but much shorter quiescent periods (eg. V1G0 between lookback times of $\sim 4 - 6$ Gyrs). Though we expect the general picture of disk formation to be similar across all our disks, a long quiescent period allows a much clearer characterization. The second-best galaxy for study appears to be V10G1 with

a quiescent disk formation period between lookback times of $\sim 2-6\,\mathrm{Gyrs}$, which is comparable to V4G0. Of the two, however, V4G0 is much more Milky-Way-like in its total stellar mass and rotation curve (see Fig 2.3). Though, as previously noted, these are not intended to be direct models of the Milky Way, it will be the subject of our eventual comparison to observations, and so we select the galaxy that is more comparable to it.

Thus we work with the disk of V4G0 between the lookback times of 8 and 4 Gyrs. Stellar properties as a function of age will hereafter be measured based on their values at $t_{lb} = 4$ Gyrs (t_4) rather than the end of the simulation at $t_{lb} = 0$ Gyrs (t_0), though their 'ages' will still be indicated as if at t_0 for consistency with earlier figures.

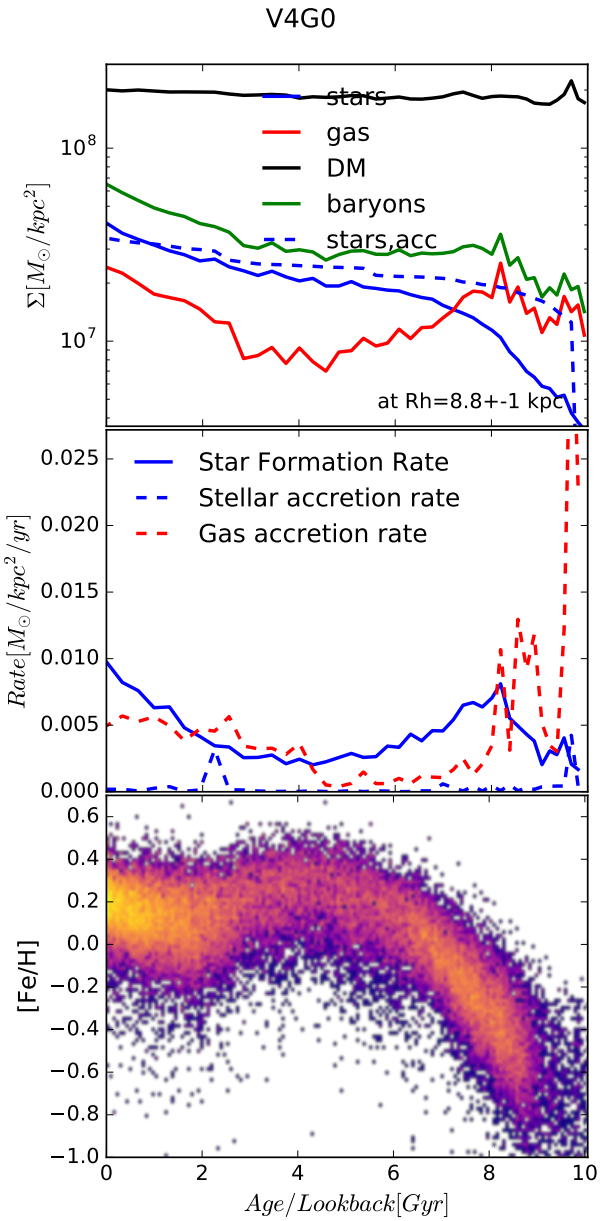

Figure 2.6: Local properties over lookback time and age for V4G0, as measured within $R_h = 8.8 \pm 1\ kpc$. The top two panels show total mass and accretion rates within this annulus for each matter component (dark matter, stars, and gas) as a function of lookback time ($t_{lb} = 0$ is end of simulation, on the left side of the x-axis). The bottom panel shows the distribution of metallicity of the stars as a function of stellar age at the end of the simulation.

Chapter 3

Vertical Structure of the Isolated Disk

In this chapter we examine the formation of the disk in the simulated galaxy identified in Chapter 2. Our aim is to understand the mechanisms responsible for setting its vertical structure and to construct a physical model of these mechanisms that can be used to interpret the origin of its vertical structure.

3.1 Disk Formation

We first take a qualitative look at the properties of the disk over the quiescent period (ie. $4 < t_{lb}/Gyr < 8$), in order to gain a general understanding of how the gaseous and stellar disks form and evolve, as well as to more specifically characterize the vertical structure of the disk during this time.

3.1.1 Inside-Out and Upside-Down

Fig 3.1 shows projections of the stellar and gaseous components of the disk, at four times, starting before the disk begins to form and throughout the period of quiet disk formation. By lookback time $t_{lb} = 8\,\mathrm{Gyr}$ the gas has collapsed into a well-defined co-planar structure, marking the beginning of the formation of the disk, which gradually grows radially and thins vertically over time. Star formation rates, shown in the two bottom rows, are by construction tied directly to higher gas densities, so the stellar disk component traces the evolution of the densest regions of the gaseous disk. The radial size of both the stellar and gaseous components grow over time, indicative of a disk that is forming inside-out.

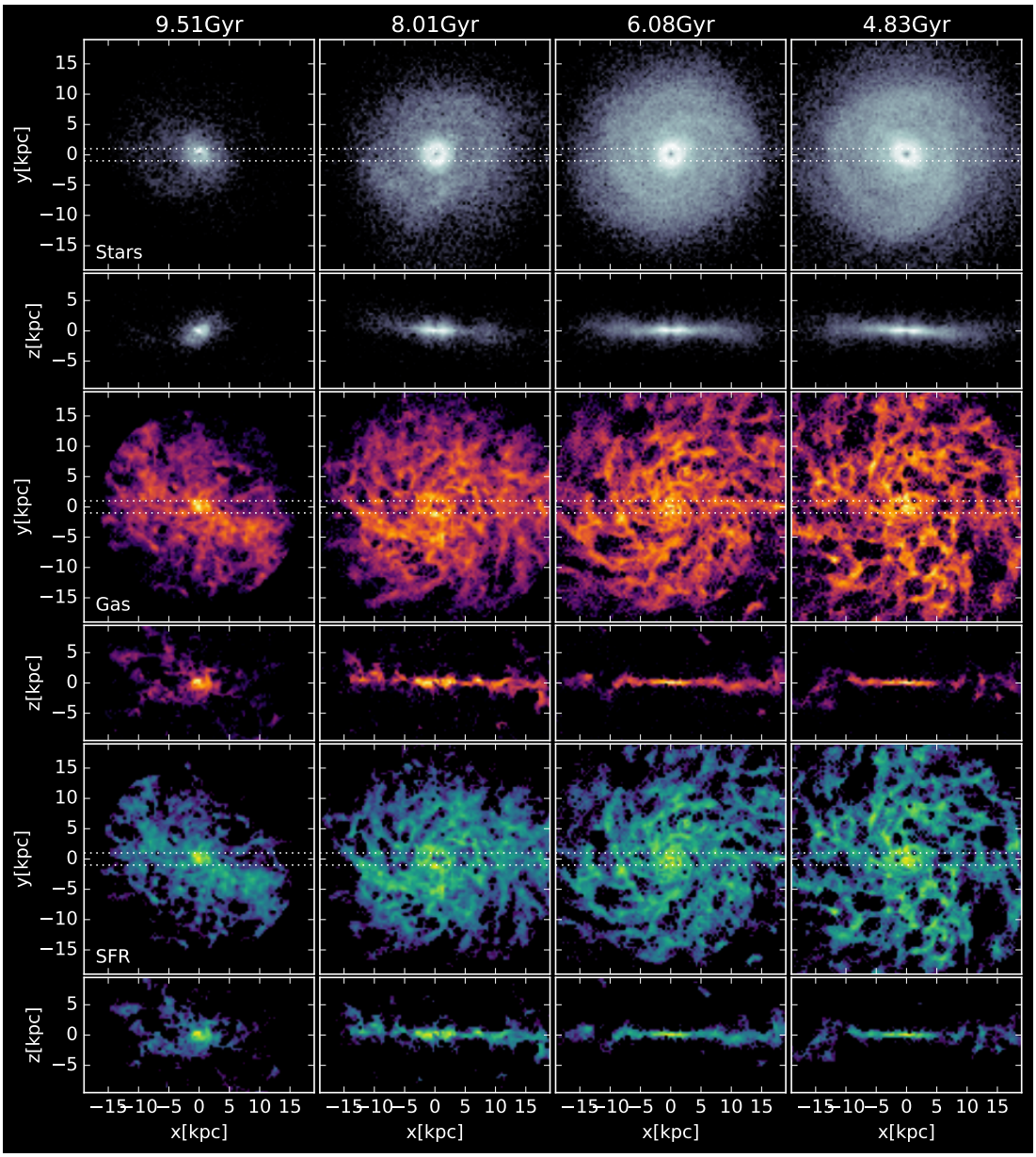

Figure 3.1: Face-on and edge-on projections of V4G0 for the mass distribution of stars with $\epsilon_j > 0.75$ (top), mass distribution of gas (middle), and its star formation rate (bottom) at four different lookback times (indicated at the top of each column). Edge-on projections are for a $\pm$1kpc slice along the y-axis, indicated by dashed lines in the face-on panels.

Cylindrical radius (R) vs vertical height (z) projections of the galaxy at these same times are shown in Fig 3.2. The top row shows the mass density of star-forming gas (SF gas) at the given lookback time, whereas newly-formed (young) stars are shown in the middle row. The bottom row shows the same stars, but at the end of the quiescent period identified in the previous chapter, which corresponds to $t_{lb} = 4\,\mathrm{Gyr}$. Note that we define 'young' stars at a given lookback time as the stars that have formed in the preceding $\sim 10^8$ years.

The gaseous disk thins gradually over time, and is clearly flared at all times (ie. the vertical thickness of the disk increases with radius). The young stellar disk as a function of time follows the same behaviour, as newly formed stars inherit the properties of their parent gas particles at the time of formation. Interestingly, the stars binned by age at t_4 are also flared, with successive age cohorts showing the same gradual thinning as the gaseous disk. There appears to be no overall change in the properties of age cohorts in the stellar disk since birth, suggesting that final stellar disk properties as a function of age are largely set at formation (we will show this in more detail in Section 3.1.2).

The result of this process is shown at t_4 in Fig 3.3, where we show the radial profiles of the vertical velocity dispersions and half-mass heights of stars binned as a function of age. Here we see explicitly the flaring of mono-age populations, as well as the gradual thinning apparent in both half-mass height and velocity dispersion. Metallicities increase monotonically over time for younger stars at all radii as a result of gradual enrichment from the ongoing in-situ star formation.

This is characteristic of a disk that is forming 'upside-down'. The stellar disk forms from a gaseous disk that is gradually thinning and enriching over time, which naturally produces age gradients as the stars inherit and preserve the kinematic and chemical properties of the gas over time.

The resulting density profiles of the galaxy at t_4 are shown in Fig 3.4. The stellar component is split into a disk ($\epsilon_j > 0.75$) and a spheroid ($\epsilon_j < 0.75$) according to the circularity parameter ϵ_j introduced in Section 2.2.1. We see from this figure that the stellar spheroid is centrally concentrated, and the stellar disk is more radially extended and the mass fraction of gas increases with increasing radius. The measured half-mass heights of stars of all ages in the disk show that the combined flaring of the mono-age populations produces a total disk density profile that is itself flared.

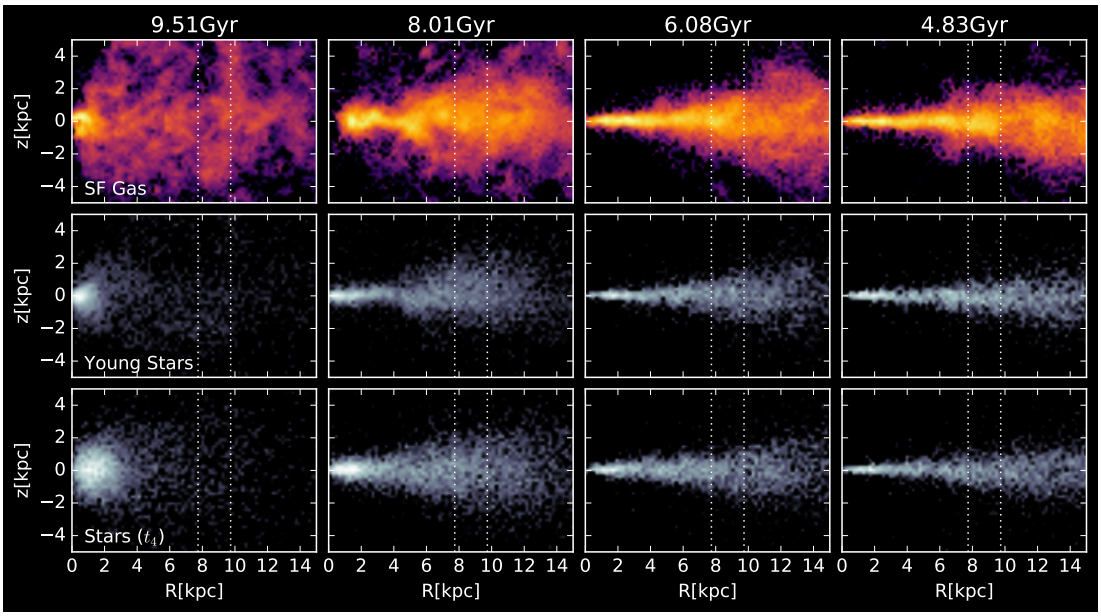

Figure 3.2: Height vs Radius mass histogram for star-forming gas (top) young stars (middle) and the same stars of the appropriate age at t_4 (bottom) at the same four times as in Fig 3.1. The vertical lines show the radial selection for properties shown in Fig 3.5.

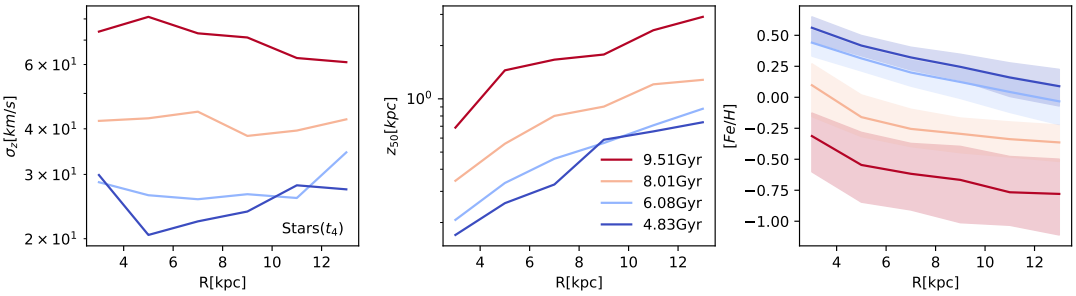

Figure 3.3: Vertical velocity dispersion (left), half-mass height (middle), and median metallicity (right) gradients for stars as a function of age at t_4 (as in the bottom row of Fig 3.2) in the same four age bins as in Figs 3.1 and 3.2. Shaded regions on the right plot show the 1σ percentile range.

3.1.2 Vertical Properties by Time and Age

We noted earlier that in Fig 3.2 there appeared to be no major difference in the kinematics and spatial distribution of the stars at the time of formation and at the end of the quiescent period at t_4. We examine this explicitly in Fig 3.5, where the disk properties over time are measured in a single radial bin about the half-mass radius R_h (the extent of this bin is shown by the dotted white lines in Fig 3.2). Red curves

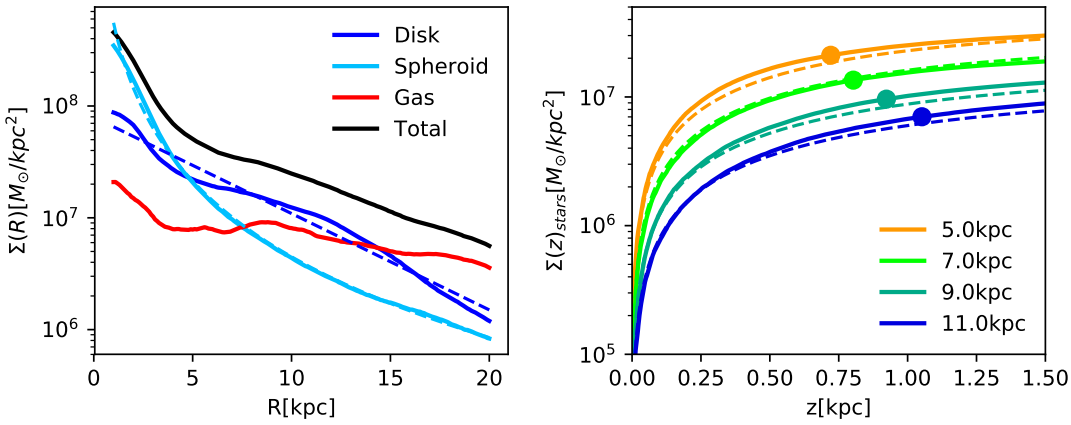

Figure 3.4: Properties of V4G0 at t_4. Left: Measured radial surface density profiles (solid lines) of gas and stars (subdivided into morphological components by circularity as in Fig 2.2). Dashed lines are fits to the spheroidal component (Sersic profile with $\Sigma_0 = 2.06 \cdot 10^8\,\mathrm{M_\odot kpc^{-2}}$, $R_e = 1.67$kpc and $n = 10.8$) and disk component (exponential profile with $\Sigma_0 = 7.95 \cdot 10^7\,\mathrm{M_\odot kpc^{-2}}$, and $R_e = 5.04$kpc). Right: Measured cumulative vertical stellar surface density profiles $\Sigma(< |z|)$ (solid lines) of the disk component at several radii with total stellar half-mass heights indicated as points. Dashed lines are expected values for an exponential vertical density profile using the measured midplane densities and half-mass heights.

show the properties of the gas component as a function of time, while the stellar component is shown in blue. For the latter, solid curves correspond to the young stellar disk at that time, whereas dashed curves indicate the properties *at* t_4 of stars as a function of age.

In the top row we again see the clear signature of upside-down disk formation: the star-forming gaseous disk (red line) gradually thins over time (measured by the decrease in both half-mass height z_{50} and vertical velocity dispersion σ_z) and the young stars (dashed blue line) inherit these properties as they form.

During this time we also see a gradual decrease in the star formation rate. This is expected, as we selected this time period because it has a minimum of gas accretion. Star formation rates depend on the amount of available gas, and no new gas is replenishing the mass being consumed to form stars, so star formation drops because of the decreasing local gas reservoir (see top panel of Fig 2.6). Metallicities increase monotonically during this time, as ongoing star formation enriches the ISM and no pristine gas is accreted to dilute it.

Of particular importance is that there is little difference between the properties of the

gas and young stars over time and those of stars as a function of age. The vertical velocity dispersion, half-mass height, metallicity distribution, and age distribution are preserved for a given age cohort, implying that migration or vertical heating have not had a significant effect on the vertical structure of the disk. This is a key property of our simulated disk, as it allows us to infer the properties of the gaseous disk over time directly from stellar properties measured at t_4 as a function of age.

Note that there is a sharp increase in the dispersions and scale heights at $t_{lb} = 4\,\mathrm{Gyrs}$, which coincides with the gas accretion event that defines the end of the quiescent period of disk formation. This further justifies our choice of time interval, as it clearly deviates from the prior pattern of isolated disk formation.

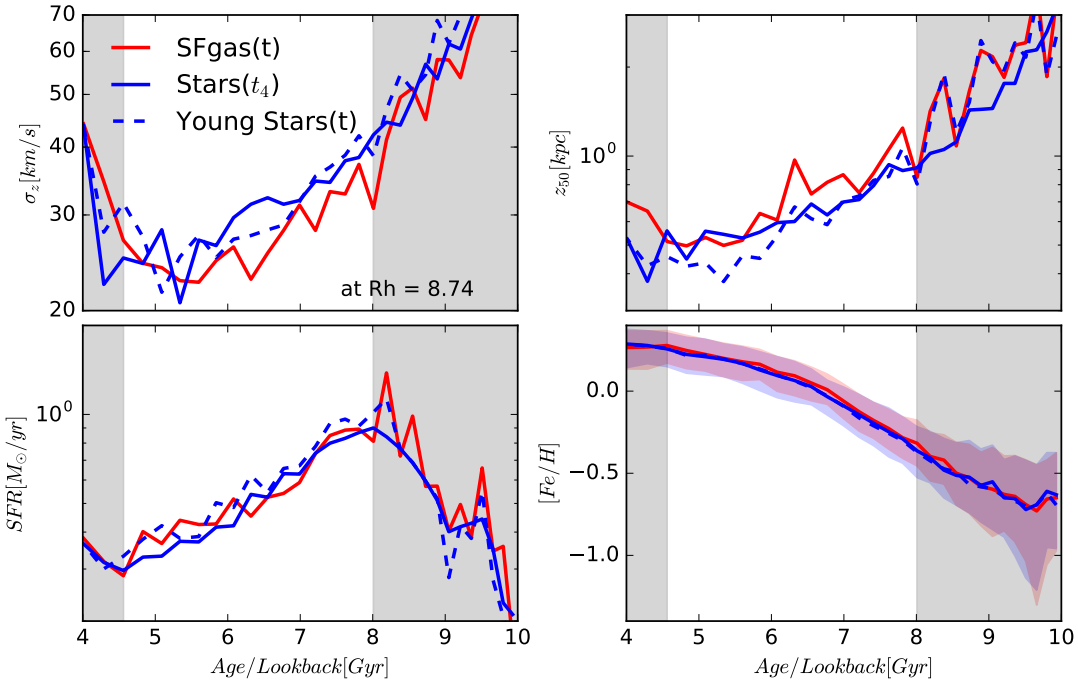

Figure 3.5: Disk properties as a function of time, or age at t_4, measured in an annulus $\pm$1kpc about R_h. Top row are measures of the vertical disk structure: the vertical velocity dispersion σ_z (top left) and the half-mass height z_{50} (top right). Bottom left is total star formation rate in the annulus, and bottom right are median metallicities. Greyed areas indicate the range outside of the quiescent period defined in Chapter 2. Plotted together in each panel are the properties of the star-forming gas as a function of time (red), the newly-formed stars as a function of time (dashed blue), and the stars as a function of age at t_4 (solid blue). The shaded regions on the bottom right are the 1σ percentile range for SFgas(t) and Stars(Age).

In summary, our stellar disk in isolation forms upside down from a flared gaseous disk that is gradually thinning and enriching over time, with star formation rates decreasing concurrently due to the transformation of gas into stars and the relatively minor gas accretion that the disk experiences over that period. The vertical structure of the stellar disk experiences no significant change after formation, so that stars of different ages at t_4 accurately trace the properties of the gaseous disk as a function of time.

With this understanding we now want to determine *why* the disk is thinning. What mechanisms are responsible for the gradual thinning over time? What parameters are needed to fully describe the vertical structure? We begin by constructing a physical model of the vertical density profile of the disk.

3.2 Modelling the Disk

We now construct a physical model of the vertical structure of the disk, which can be applied to other observed systems. To begin with, there are a number of initial insights we can explore based on the measured disk properties we have seen thus far. Firstly, vertical crossing times in the disk are short ($\sim 10^7$ years for $z_{50} \sim 1$ kpc and $\sigma_z \sim 30$ km/s) compared to the Gyr timescales of gradual thinning seen in Fig 3.5. There must therefore be a restoring pressure supporting the disk against the vertical acceleration due to gravity, else it would collapse much more quickly than we observe. This suggests that the gaseous disk is in quasi-hydrostatic equilibrium at all times and that the gradual thinning is being regulated by a process working on longer timescales.

Secondly, we know that this restoring pressure must come from two sources: the thermal pressure of the gas (which depends on the hydrothermal equation of state chosen for the simulation) and the kinetic pressure due to bulk motions. We have seen in the previous section that there is little difference between the thickness of the gaseous disk at a given time and the thickness of the stellar populations forming from it. This indicates already that the kinetic pressure is likely much more important than the thermal pressure, since if this were not the case then we would expect that newly-formed stellar populations (which are collision-less and unaffected by the thermal pressure of the gas) would collapse immediately after formation and thus be much thinner than the gaseous disk.

3.2.1 Gaseous Disk in Hydrostatic Equilibrium

With these insights in mind we proceed to derive a model for the disk, beginning with a gaseous disk in hydrostatic equilibrium for which the balance of vertical forces at a given radius can be expressed as:

$$\frac{1}{\rho}\frac{\delta P}{\delta z} = -\frac{\delta \Phi}{\delta z} \tag{3.1}$$

where ρ is the gas volume density, P is the gas pressure, z is the absolute height above the disk, and $\frac{\delta \Phi}{\delta z} = \frac{\delta \Phi_{bary}}{\delta z} + \frac{\delta \Phi_{DM}}{\delta z}$ is the combined vertical acceleration due to the potential of the baryonic disk and dark matter halo.

For a gas with a polytropic equation of state, as is used in our simulations, the thermal pressure can be expressed as:

$$P = P_{eos}\left(\frac{\rho}{\rho_{eos}}\right)^{\Gamma} = \frac{c_s^2\rho}{\Gamma} \tag{3.2}$$

where $P_{eos} = 1.10\mathrm{g\,cm^{-1}\,s^2}$ and $\rho_{eos}/m_p = 0.1\,\mathrm{cm^{-3}}$ are normalizations adopted in the EAGLE equation of state, $\Gamma = 4/3$ is the polytropic index, and $c_s = \frac{\delta P}{\delta \rho}$ is the sound speed. The sound speed can also be expressed as $c_s = c_{s,eos}(\frac{\rho}{\rho_{eos}})^{\frac{\Gamma-1}{2}}$, where $c_{s,eos} = (P_{eos}\Gamma/\rho_{eos})^{1/2} = 9.4\,\mathrm{km/s}$.
For the kinetic pressure we use the vertical velocity dispersion σ_z of the gas in place of the sound speed in equation 3.2:

$$P = \frac{\sigma_z^2\rho}{\Gamma} \tag{3.3}$$

The disk at the half-mass radius has a roughly constant midplane density of $\rho_0 \sim 0.3\,\mathrm{cm^{-3}}$ during the quiescent period, as we will see in Fig 3.7, which produces a midplane sound speed $c_s \sim 11\,\mathrm{km/s}$. When compared with measured velocity dispersions on the order of $20-40\,\mathrm{km/s}$ this means that the thermal pressure (as per Equation 3.2) is smaller than the kinetic pressure (as per Equation 3.3) by roughly a factor of $(\frac{20}{11})^2 \sim 4$ during the quiescent period. This is also consistent with our above expectation that the kinetic pressure dominates based on the similarity in vertical disk properties between the gas and stars. For simplicity we thus proceed with the derivation by expressing the pressure in terms of the kinetic pressure exclusively (we will again show this is justified when testing the model on the simulation in Fig 3.7).

We further make the simplifying assumption that the gas is "isothermal" (ie. that σ_z is constant with height). In this case our expression of hydrostatic equilibrium becomes:

$$\frac{1}{\rho}\sigma_z^2\frac{\delta\rho}{\delta z} = -\frac{\delta\Phi}{\delta z} \tag{3.4}$$

for which it is straightforward to integrate for the vertical density profile:

$$\rho(z) = C\frac{\Sigma_g}{z_{50}}e^{-\frac{\Phi(z)-\Phi(0)}{\sigma_z^2}} \tag{3.5}$$

where $C = z_{50}\int_0^\infty e^{-\frac{\Phi(z)-\Phi(0)]^{-1}}{\sigma_z^2}}dz$ is a dimensionless constant for all heights z, and

$\Sigma_g = \int_0^\infty \rho(|z|)dz$ is the total gas surface density at a given radius. Note that the z_{50} in the expression cancels out with that in C - they have been added for dimensional clarity.

3.2.2 Model Test

We now want to test Equation 3.5 and its assumptions by comparing the vertical density profile it predicts to that measured directly from the simulation. To do this we need measurements of the parameters σ_z (shown in Fig 3.5), Σ_g (shown in Fig 2.6), and the potential Φ (shown below).

We show the shape of the potential in the disk over the quiescent period in Fig 3.6, measured by the contributions from the halo and disk to the rotation curve (left panel) and to the vertical acceleration at the half-mass radius (right panel). The three times shown are the same as those in Figs 3.1 and 3.2 (the pre-disk-formation snapshot at $t_{lb} = 9.5\,\mathrm{Gyr}$ has been omitted for clarity). The last parameter needed for Equation 3.5 is the total vertical acceleration as a function of height (right panel), integrated numerically for $\Phi(z)$.

Before we move on, we must emphasize two features of Fig 3.6 that will become important in subsequent sections.
First, the potential as a function of both radius and height remains essentially constant over time, likely because this time period was chosen for having a minimum of mass accretion. As a result, the change in the density profile as a function of time is entirely dependent on the changes over time in only σ_z and Σ_g.
Second, although the vertical acceleration $d\Phi/dz$ is dominated by the halo at larger heights, the contribution from the baryonic disk becomes comparable to that of the halo closer to the midplane ($z \lesssim 1\,\mathrm{kpc}$, which is of the order of the disk half-mass heights). The contribution to the potential of both components will have to be accounted for later when we derive relations between velocity dispersion and scale height for a given potential in Section 3.3.

We test our model in Fig 3.7, which compares the predicted density profile from Equation 3.5 (dotted lines) to the measured density profile of the simulation (solid

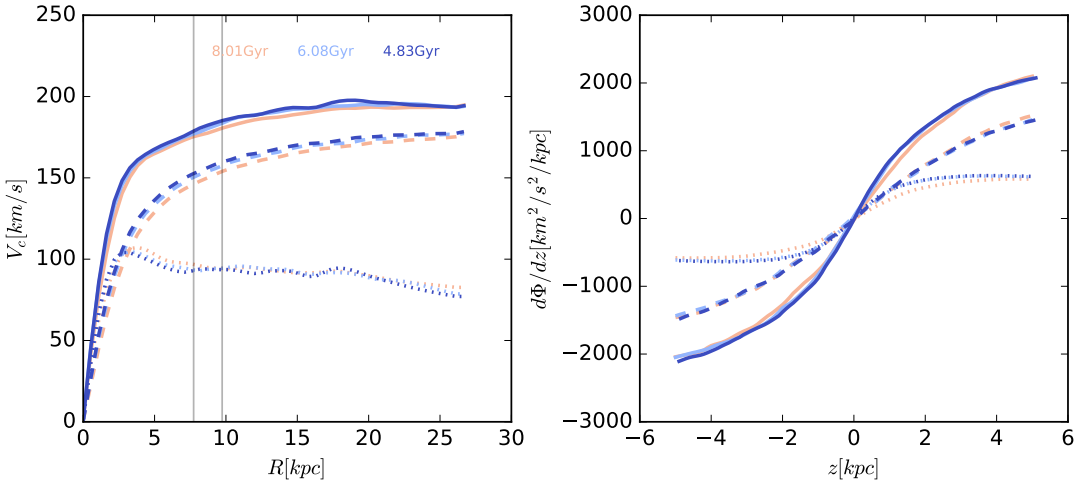

Figure 3.6: Circular velocity $V_c = \sqrt{\frac{GM(<r)}{r}}$ vs Radius (left) and the vertical gradient of the potential $\frac{d\phi}{dz}$ at the half-mass radius (right) for the galaxy at the same lookback times as in Figs 3.1 and 3.2 (excepting the pre-disk snapshot at $t_{lb} = 9.5$ Gyrs). The vertical lines on the left show the radial bin about the half-mass radius R_h in which we measure the vertical acceleration shown on the right. The totals (solid lines) are divided into contributions from the dark matter (dashed) and baryons (dotted). During the quiescent period the potential changes very little over time.

lines). The times shown are the same as in Fig 3.6. We have also included the predicted profile if the thermal pressure (Equation 3.2, dashed lines) is the sole restoring force instead of the kinetic pressure. The predicted density profile using only the kinetic pressure clearly recovers the measured density profile at all three times, as we expected based on earlier observations, in contrast with that using the thermal pressure which significantly overpredicts the midplane density while underpredicting the overall thickness.

3.2.3 Summary

We conclude that our model of a gaseous disk in hydrostatic equilibrium, dominated by an isothermal kinetic pressure due to bulk motions of the gas, provides an accurate description of the vertical structure of the simulated gaseous disk. The vertical density profile of the gas at a given time can thus be recovered if the vertical velocity dispersion σ_z, the gas surface density Σ_g, and the shape of the potential Φ are known.

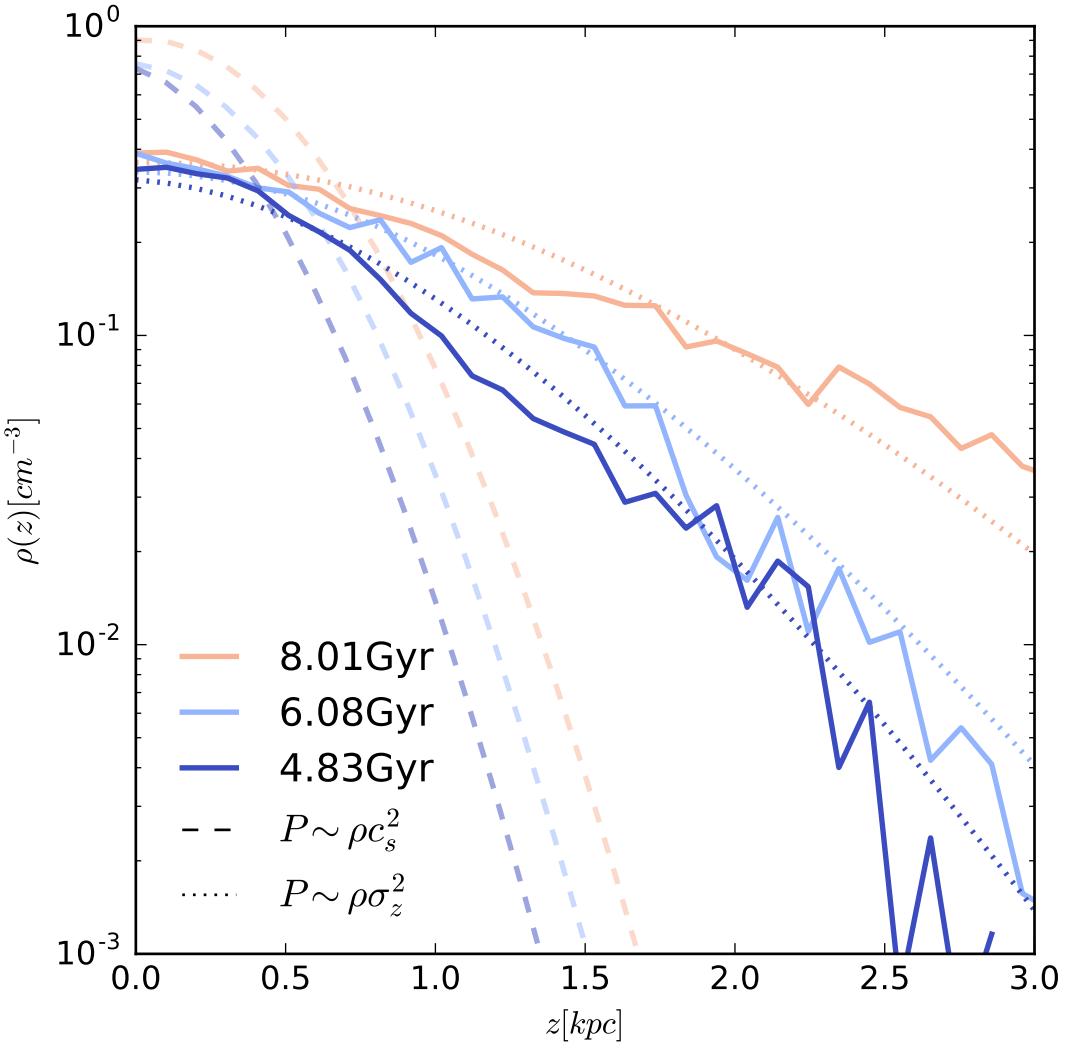

Figure 3.7: Vertical density profiles at different lookback times (same times as Fig 3.6). Solid lines are the measured densities from the star-forming gas. The other lines are predictions using eq (3.5), where the dashed lines assume the gas is primarily supported by the thermal pressure (c_s) and the dotted lines by kinetic pressure (σ_z).

In the following sections we make use of this in two ways to obtain predictive results that can be applied to observed systems.
The first is to use analytical expressions in a thin disk approximation for the vertical acceleration of the halo and disk $\delta\Phi/\delta z$ in Equation 3.4, rather than computing it directly as we did for Fig 3.5. This will provide a relation between velocity dispersion σ_z and scale height z_h in terms of disk properties that are more readily measurable, such as the rotation curve and the surface density of the disk, which can serve as a diagnostic for the applicability of our model to an observed stellar disk.
The second is to examine explicitly the thinning of the disk over time, building off of our earlier observations that σ_z and Σ_g are the only time-dependent properties in our vertical density profile, and that vertical properties of stellar populations are preserved over time. This will allow us to relate stellar properties measured as a function of age (namely an age - velocity dispersion relation) to the properties of the gaseous disk as a function of time.

3.3 σ_z vs z_{50} in a Thin Disk

We begin with the first approach, in which we take analytic expressions for $d\Phi/dz$ in place of a direct measurement in Equation 3.4, and derive the resulting scale height z_h in terms of the vertical velocity dispersion σ_z. Note that for this section we refer to the work of Benítez-Llambay et al. (2018), who examined the vertical properties of polytropic gaseous disks embedded in a CDM halo.
The expressions for a disk whose potential is dominated by a thin baryonic disk (SG: self-gravitating) or the dark matter halo (NSG: non-self-gravitating) will be considered separately to start, and a combined solution in the case where they are comparable, which we observed to be the case in our simulated disk in Fig 3.6, will be presented later.
Note that we begin with a purely gaseous disk, and then for each case (SG, NSG) adjust the expressions where necessary to apply to a stellar disk with individual sub-populations.

3.3.1 Non Self-Gravitating

For a non-self-gravitating disk in a thin disk approximation ($z/R << 1$), the contribution of the dark matter halo to the vertical acceleration is expressed as:

$$\frac{\delta\Phi_{DM}}{\delta z}(R,z) = -\frac{V_{DM}^2(R)\,z}{R^2} \tag{3.6}$$

where V_{DM} is the contribution of the halo to the rotation curve. Substituting this into our expression for an isothermal disk in hydrostatic equilibrium (HSE) (Eq 3.4) we get:

$$\frac{1}{\rho}\frac{\delta\rho}{\delta z} = -\frac{1}{\sigma_z^2}\frac{V_{DM}^2(R)z}{R^2} \tag{3.7}$$

which we integrate to obtain the density profile

$$\rho(R,z) = \rho(R,0)\exp -(\frac{z}{z_{h,NSG}})^2 \tag{3.8}$$

where $z_{h,NSG}$ is the non self-gravitating scale height,

$$z_{h,NSG} = \sqrt{2}\frac{\sigma_z}{V_{DM}}R \tag{3.9}$$

Thus for a non-self-gravitating disk we expect that scale height $z_{h,NSG}$ will scale linearly with σ_z ($z_{h,NSG} \sim \sigma_z$). This result for a gaseous disk is equally applicable to a stellar sub-population embedded in a thicker disk, since in both cases the gravity due to the dark matter halo is the same. Thus we can also apply Equation 3.9 as written to individual stellar sub-populations.

3.3.2 Self-Gravitating

In the self-gravitating case, the contribution of a thin disk to the vertical acceleration is:

$$\frac{\delta\Phi_{bary}}{\delta z}(R,z) = -2\pi G\Sigma(R,z) \tag{3.10}$$

where $\Sigma(R,z) \equiv 2\int_0^z \rho(R,z')\delta z'$ is the surface density profile of the disk. We can express this in terms of the surface density only to obtain:

$$\frac{\delta P}{\delta\Sigma}(R,z) = -\pi G\Sigma(R,z) \tag{3.11}$$

which when integrated returns

$$P(R,z) = P(R,0)(1 - \frac{\pi G\Sigma_z^2(R,z)}{2P(R,0)}) \tag{3.12}$$

This defines a scale height $z_{h,SG}$ where the pressure (and thus density) drops to zero, such that

$$\Sigma(R, z_{h,SG}) = (\frac{2P(R,0)}{\pi G})^{\frac{1}{2}} \tag{3.13}$$

If we assume that the density profile has the same functional form as for the NSG solution (Eq 3.8), and recalling that given the isothermal assumption $P(R,0) = \rho(R,0)\sigma_z^2$, then we can recover the self-gravitating scale height:

$$z_{h,SG} = \frac{2\sigma_z^2}{\pi^{3/2} G \Sigma(R)} \tag{3.14}$$

where by construction $\Sigma(R) = \Sigma(R, z_{h,SG})$ is the total surface density of the disk at radius R.

Unlike the non-self-gravitating case, this cannot be directly applied to a stellar sub-population. In the self-gravitating case we must account for the fact that the density profile of a stellar sub-population may not describe the total density profile of the stellar disk. Equation 3.14 holds for a purely gaseous disk, or for a disk where every stellar population at a given radius has the same scale height. However, in the case where we have a thin stellar population embedded within a thicker disk, such as a young stellar population in a gradually thinning disk, the effective self-gravitating potential felt by the thinner population will be different than for a thicker one.
We account for this by replacing the total surface density $\Sigma(R)$ in Equation 3.14 with an effective surface density $\Sigma(R, z_h) = 2\int_0^{z_h} \rho(R, z')dz'$ and solving for the resulting scale height numerically. This requires prior knowledge (or an assumption) of the shape of the total vertical density profile $\rho(R, z)$, which for the simulation we can either measure directly, or assume to be a simple exponential according to the successful application of Equation 3.5 to the disk in Fig 3.7. Thus, when applied to a single stellar population our equation becomes:

$$z_{h,SG} = \frac{2\sigma_z^2}{\pi^{3/2} G \Sigma(R, z_h)} \tag{3.15}$$

Note that in the purely gaseous case of Equation 3.14, we expect self-gravitating height to scale as $z_{h,SG} \sim \sigma_z^2$, but that this is not necessarily the case when applied to stellar sub-populations with Equation 3.15, which has an additional $z_{h,SG}$ in the

surface density term $\Sigma(R, z_h)$. While thicker populations with larger scale heights will converge to the $z_h \sim \sigma_z^2$ scaling of Equation 3.14, thinner sub-populations will scale non-linearly with σ_z. This will cause a shallower trend in z_h with decreasing σ_z than would be expected for a purely gaseous disk, as we will see shortly in Section 3.3.4.

3.3.3 Combined Solution

In the case where the contributions to the potential from the halo and the disk are comparable (which as we saw in Fig 3.6 is the case for our simulated disk) then the actual scale height of the disk will be smaller than either of those predicted by the SG and NSG solutions independently. The final scale height can be approximated with:

$$\frac{1}{z_h^2} = \frac{1}{z_{h,NSG}^2} + \frac{1}{2\, z_{h,NSG}\, z_{h,SG}} + \frac{1}{z_{h,SG}^2} \tag{3.16}$$

where $z_{h,NSG}$ and $z_{h,SG}$ are given by equations 3.9 and 3.15 respectively.

Finally, we can convert these scale heights to a characteristic half-mass height z_{50} by simply integrating the functional form of the density profile (eg. Eq 3.8) to the desired surface density fraction. In our isothermal case this conversion is $z_{50} = 0.477 z_h$ (see Benítez-Llambay et al. (2018) Table 1 for a breakdown with different values of Γ).

3.3.4 Application to Simulated Disk

Fig 3.8 shows the application of Equations 3.9 and 3.15 to the stellar populations in our simulated disk, using the measured rotation speed and vertical density profile directly (as shown in Figs 3.6 and 3.3).

In the left panel we show the measured z_{50} vs σ_z for stellar mono-age populations (circles) as a function of radius, with a running mean of the points to more clearly show the trend. All radii behave similarly, scaling approximately as $z_{50} \sim \sigma_z$. In the right panel we focus on two of these radii (3 kpc and 9 kpc to represent the inner and outer disk respectively) and show the predicted relations based on the individual contributions from the SG (Eq 3.15) and NSG (Eq 3.9) components, as well as their combined contribution following Equation 3.16. To highlight the effect of the

adjustments we made to the SG solution to apply to thin stellar populations, we also include the combined solution if Equation 3.14 is used in place of Equation 3.15 for the SG component as a faded solid line.

We expect that the gravity of the halo should dominate in the outer disk, and that the self-gravity of the disk should become increasingly important with decreasing radius. For a *gaseous* disk we expect this to cause heights to scale as $z_{50} \sim \sigma_z$ at large radii, and gradually shift to $z_{50} \sim \sigma_z^2$ at small radii, such that for a fixed range in σ_z the trend of z_{50} vs σ_z should become increasingly steep with decreasing radius. However, for populations in a *stellar* disk, where we must account for total thickness, this is not the case.

We can see this in the measured stellar populations from the simulation (left panel), where all radii scale similarly in the same σ_z range (approximately as $z_{50} \sim \sigma_z$ throughout). The reason for this becomes clear in the right panel, where we compare our predicted relations to the two example radii (running means are reproduced from the left panel). The prediction for a purely gaseous disk using Equation 3.14 for the SG component (faded line) still matches the measured outer disk at 9 kpc where the NSG component dominates, but in the inner disk at 3 kpc it predicts a steeper relation at lower σ_z than is measured. Properly accounting for a thin stellar population in an overall thicker disk with Equation 3.15 (darker solid line) makes the relation shallower at lower σ_z, and better matches the measured values in regimes where the disk's self-gravity dominates.

Thus we expect that in a stellar disk all radii should scale similarly (approximately $z_{50} \sim \sigma_z$), and we see that the predicted relation using Equation 3.15 for the SG component accurately predicts the measured properties at both outer and inner radii.

To summarize the section, we have derived a relation that predicts the scale height of an isothermal stellar population in quasi-hydrostatic equilibrium, given its velocity dispersion, as a combined function of the gravitational accelerations from the dark matter halo and the self-gravity of the disk. By comparing the predicted scale heights to those of observed stellar populations, we can test these conditions (isothermality and dynamic equilibrium) for that population.

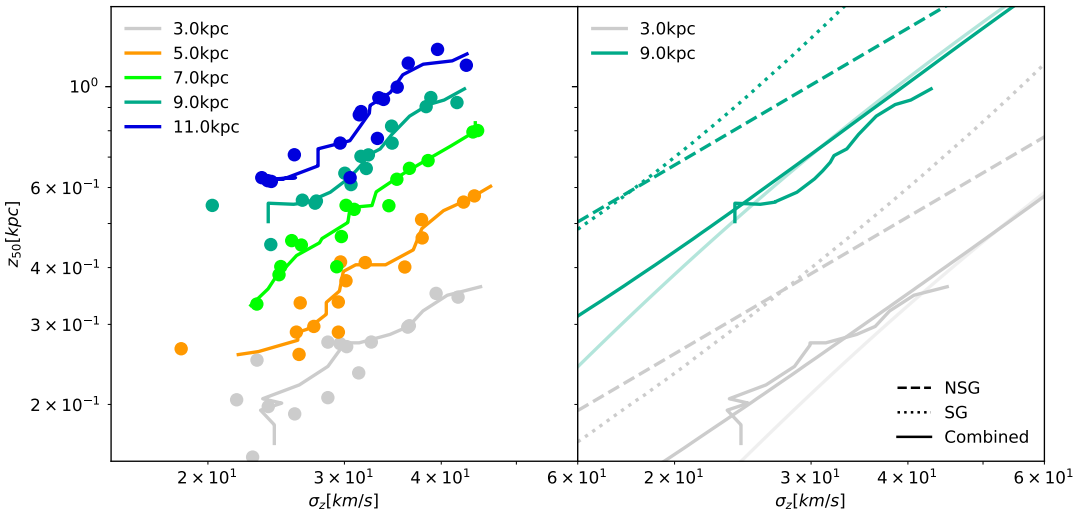

Figure 3.8: Left: Measured z_{50} vs σ_z of stars as a function of age for the quiet period over multiple radii (points). Lines are running medians. Right: Running median of two example radii (3 kpc, 9 kpc) together with the predicted relation for the NSG (dashed, Eq 3.9), SG (dotted, Eq 3.15), and combined (solid, Eq 3.16) analytical solutions. The faded lines show the combined solution *without* the correction made to the SG component accounting for a stellar disk (see text).

3.4 Velocity Dispersion and Star Formation

Finally, we explore what mechanisms regulate the gradual thinning of the gaseous disk in our simulation, and what determines the origin of vertical structure in the stellar disk.

First, recall the observation made in Section 3.2.1, where, for a constant potential, the time dependence of the vertical velocity dispersion is entirely described by the time dependence of the surface density of the gas. This gas surface density is directly related to the surface density of star formation Σ_{SFR} by construction in our simulations (see Section 2.1.5), meaning that *the local thinning of the disk over time is directly linked to the local decrease in star formation rate.*
We show the relations between these parameters at R_h over the quiescent period in Fig 3.9. The left panel shows our measures of the gas surface density (triangles) and star formation rate, which we can see closely follow the Kennicutt-Schmidt law approximated by the star formation algorithm implemented in EAGLE. This confirms our above statement that if $\sigma_z(t) \propto \Sigma_{gas}(t)$ then $\sigma_z(t) \propto \Sigma_{SFR}(t)$. We have also included the total baryon surface density ($\Sigma_{gas} + \Sigma_{stars}$) (squares) to again highlight its constancy over the quiescent period, such that the gas density decreases due to active star formation and is not being replenished by external sources.
The right panel shows the relation between $\sigma_z(t)$ and Σ_{SFR} for young stars over time, where we see that once the disk begins to form ($t_{lb} < 8\,\mathrm{Gyrs}$) these quantities are clearly correlated: as star formation rates decrease the vertical velocity dispersion of newly-forming stars decreases accordingly.

We expect that the feedback from star formation must play an important role in moderating disk thickness. Without feedback the bulk motions in the disk should settle on a dynamical timescale, which based on the rotation speed at our disk's half-mass radius (see Fig 2.3) is of the order of $\sim 10^8$ years. Given that the disk continues to collapse while dominated by the bulk motion of the gas for up to 4 Gyrs, it is clear that feedback *must* be responsible for supporting the vertical velocity dispersion over time.
Thus, as the gas is consumed to form stars, and no new gas is accreted to replenish local reservoirs, the local star formation rate drops. This reduces the energy returned to the ISM by feedback, and the vertical motions of the gas decrease according to the

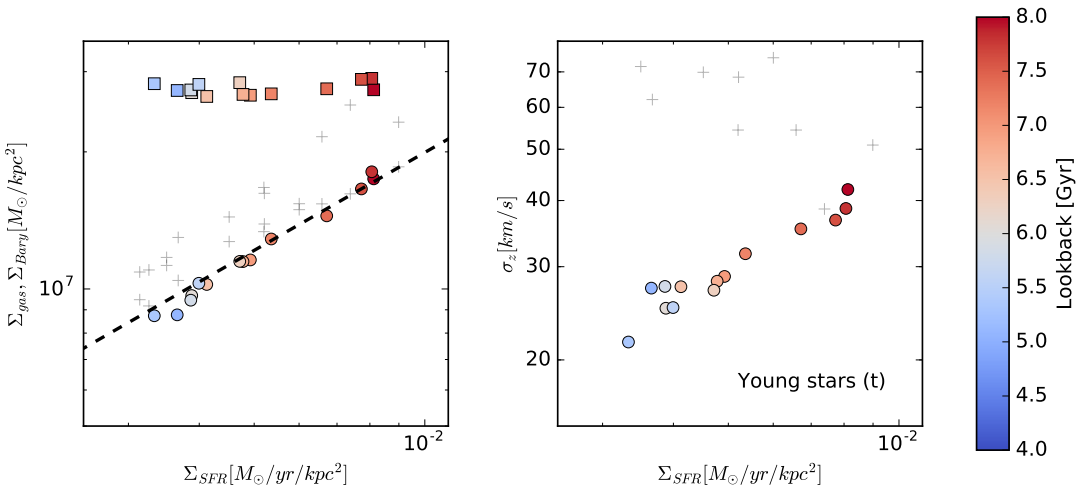

Figure 3.9: Surface density of star formation rate plotted against mass surface density (left) and velocity dispersion (right) measured in the $R_h \pm 1\,\mathrm{kpc}$ annulus. In both panels, the points are coloured by lookback time, covering the time range of the quiescent disk formation period defined in Chapter 2, and points before this period ($t_{lb} > 8\,\mathrm{Gyrs}$) are marked as grey crosses. In the left panel, the squares are $\Sigma_{baryons}$, while circles are Σ_{gas}. The black line shows the Kennicutt-Schmidt relation with parameters (A=$1.515 \cdot 10^{-4} M_\odot/yr/kpc^2$, n=1.4), which is used as the basis for star formation in EAGLE (Schaye et al., 2015). In the right panel we plot the values measured for newly-formed stars over time, as done previously in Fig 3.5.

trend seen in Fig 3.9. Newly-formed stars inherit the vertical properties of the gas over time, and a preserve them until the end of the quiescent period.

This means that in our simulation there is a measurable, predictive connection between the age-velocity dispersion relation and the star formation history at a given radius in the disk. We show in Figs 3.10 and 3.11 (where we have reproduced elements of Fig 3.5 and 3.9 as a function of radius) that this behaviour is consistent across multiple radii, and not exclusive to R_h.
The right panel of Fig 3.11 shows the σ_z-Σ_{SFR} relations for multiple radii normalized to their final values at t_4. We fit a simple power law of the form $\frac{\Sigma_{SFR}(t)}{\Sigma_{SFR}(t_4)} \sim (\frac{\sigma_z(t)}{\sigma_z(t_4)})^n$ to the data points shown for all radii together using an MCMC method. This returns a fitted power-law index $n = 1.82$ with a 1σ confidence interval of $[0.93, 2.71]$, plotted as the dotted line on top of the data. Despite the wide interval, this provides an acceptable fit to the data, and is clearly equally valid at all radii. This empirical fit captures in a simple way the complex relationship between cooling, star formation, feedback, and the resulting vertical structure in the simulation.

This is a central result of this work. In a disk that has had a relatively unchanging potential over time and no major source of vertical heating, at a given radius the local AVR and current star formation rate (both readily observable) can be used to recover the local star formation history. Lacking a net redistribution of stars to other radii, this can also be integrated to predict the local age distributions of the disk.
We show an example of how this can be used in Fig 3.12, where we have taken these quantities and applied the fitted power law index n to convert the scaling of the AVR as a function of age to the scaling of the star formation rate as a function of time to produce a predicted cumulative age distribution at a given radius. This recovers the measured age distribution at t_4, and it can in principle be easily applied to the Milky Way (as we will see in Chapter 4).

3.4.1 Summary

To summarize, our simulated stellar disk forms upside-down from a gradually thinning and enriching gaseous disk. The properties of the gaseous disk over time are preserved in the stars as a function of age. The rate of thinning is regulated by stellar feedback

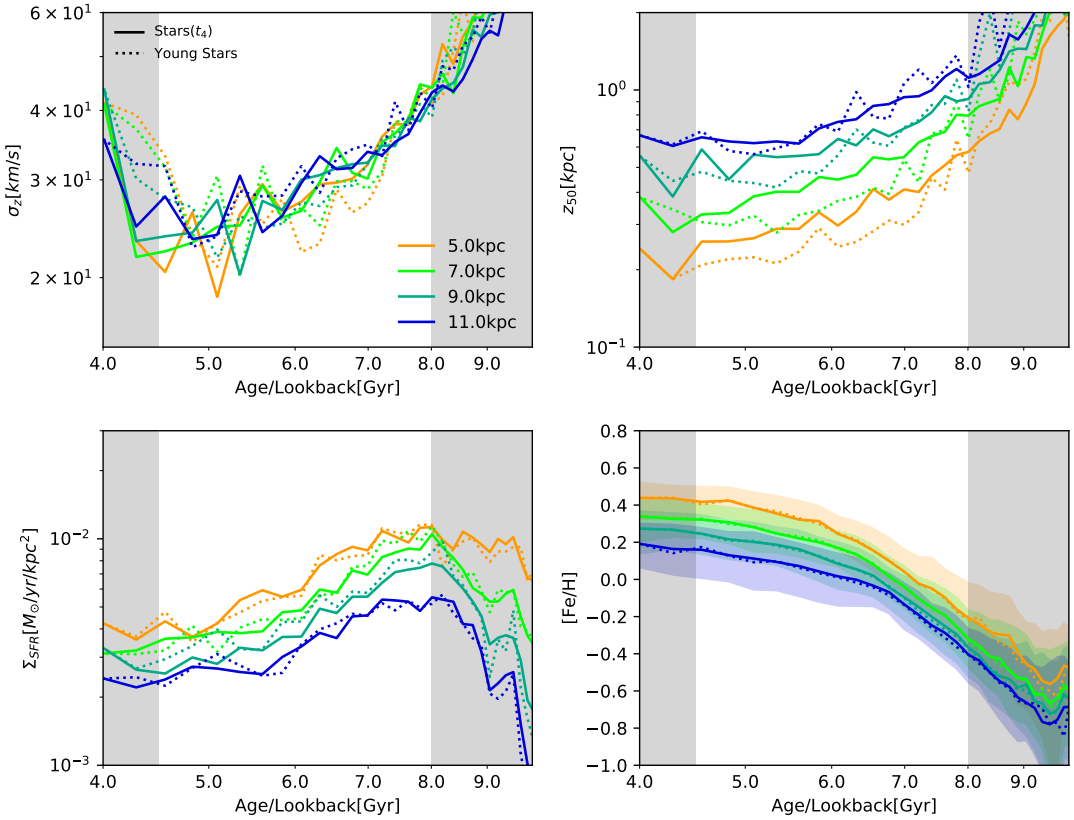

Figure 3.10: Same as in Fig 3.5 but shown over multiple radii (legend in top left panel). Solid lines are stars binned by age at t_4 while dotted lines are young stars over time. Shaded region in bottom right panel is 1σ percentile for stars by age.

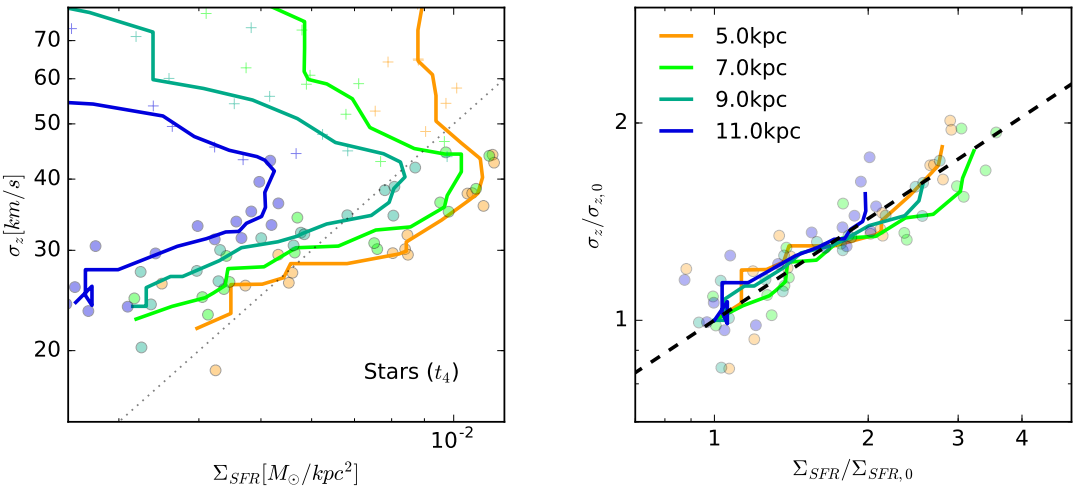

Figure 3.11: Vertical velocity dispersion of stars(age) vs star formation rate per unit area of SFgas(t) over multiple radii. Left panel points are for every snapshot from $t_{lb} = 10\,\mathrm{Gyrs}$ to $t_{lb} = 4\,\mathrm{Gyrs}$, with crosses for times before disk formation ($t_{lb} > 8\,\mathrm{Gyr}$) and circles during ($t_{lb} < 8\,\mathrm{Gyr}$). Solid lines are running medians of the points, and the dotted line shows a power law with index of n=1 to guide the eye. Right panel shows the same quantities, trimmed to the quiescent period only, and normalized to their final t_4 values. The dashed line indicates the best-fit power law relation over all radii.

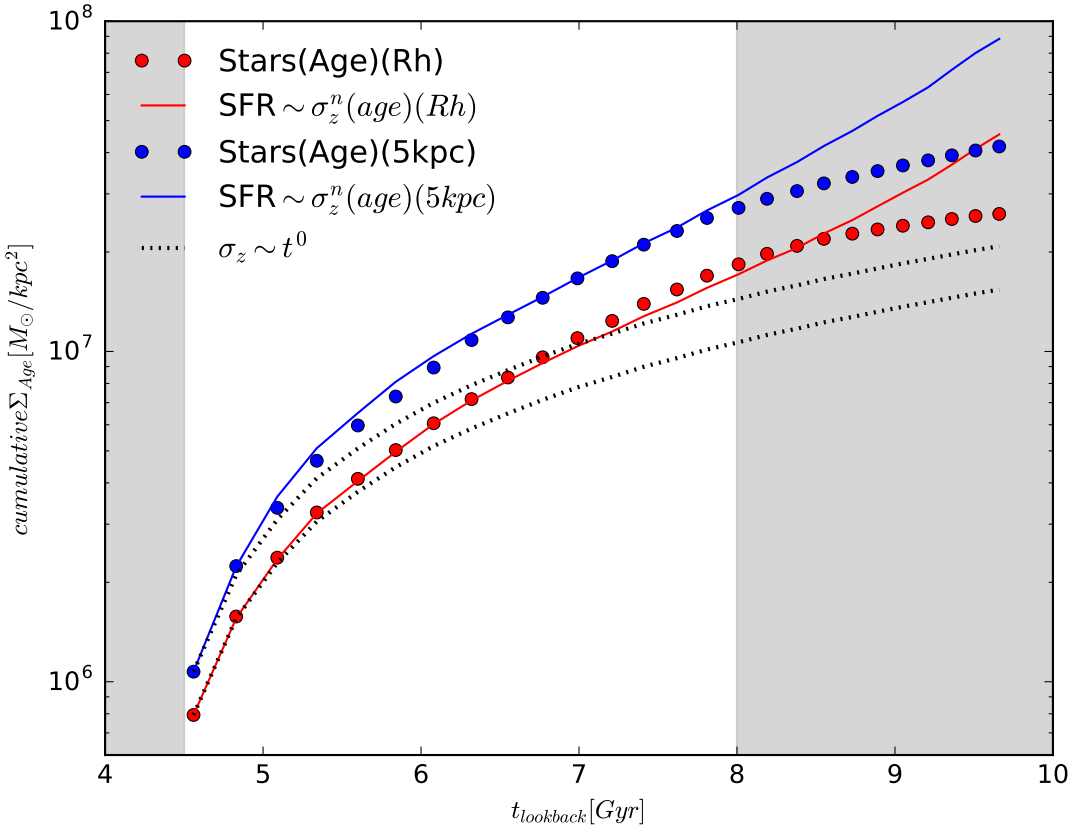

Figure 3.12: Cumulative age distributions at t_4 at two example radii (R_h in red, 5 kpc in blue). Solid lines are measured age distributions at t_4, while the points are the predicted age distributions based on the scaling of the vertical velocity dispersions using the fit shown in Fig 3.11. Dotted lines show predicted age distributions at each radius for an AVR that scales as t^0 (ie. constant) to guide the eye.

from star formation, such that the age-velocity relation at a given radius reflects the time evolution of the star formation. We also derive the relation between σ_z and z_{50} of a stellar population which depends on measurable properties of the potentials of the halo and disk. Both of these results can be applied to any observed system for which we can measure σ_z and z_{50} of stellar populations as a function of age - in the next chapter we apply this to observations of stellar populations in the Milky Way from the literature.

Chapter 4

Application to the Milky Way

In this chapter we apply the relations derived from our simulated disk in the previous chapter to observations of stellar populations in the Milky Way, in order to test whether the vertical structure of the Milky Way's disk follows a similar formation process as in our simulation. We first present the observed age-velocity dispersion relations (AVR) and scale heights taken from the literature in Section 4.1, and then apply our results (σ_z - z_{50} relations and AVR - star formation history prediction) to them in Sections 4.2 and 4.3.

4.1 Observational Data

To apply our results to the Milky Way we need stellar surveys with individual stellar age determinations, Galactocentric positions, and Galactocentric velocities. This allows us to measure the vertical velocity dispersions for stellar populations as a function of age and radius, in the same way as we have done for our simulated disk, and thus predict a local star formation history as in our Section 3.4. We also need the half-mass heights of these stellar populations, in order to test the velocity dispersion - scale height relation of the disk as in Section 3.3.

For the velocity dispersions we use the observed AVRs from Sanders & Das (2018) (SD18 hereafter) and Mackereth et al. (2019) (M19 hereafter), reproduced in Fig 4.1. Both take advantage of the second data release of the Gaia survey (Gaia DR2 (Gaia Collaboration et al., 2018)), which provides photometry and astrometry for 1.3 billion stars across a large extent of the Milky Way, to study the kinematics of the Galactic stellar disk on large scales. Importantly, both surveys are crossmatched with additional spectroscopic surveys to produce a combined catalogue of stars over a large range of radii for which they can determine individual stellar ages.

Both sources are used since neither is ideal for our needs: SD18 bin their stellar populations by age and radius, making our method directly applicable, but their youngest ages are not very reliable. This is potentially problematic since our star formation history prediction relies on scaling properties to the youngest stars. In contrast, M19's young ages are more robust, but they bin by age and metallicity (rather than by age and radius) and only report a corresponding mean radius for the binned population. We therefore use both to cover their respective shortcomings when used in our analysis.
For scale heights we use the fitted density profiles from Mackereth et al. (2017) (M17 hereafter), who fit exponential scale heights as a function of radius to stellar populations binned by age and metallicity similarly to their M19.
We describe each of these sources in some detail below.

4.1.1 Sanders+2018

Sanders & Das (2018) (SD18) crossmatch photometric and astrometric properties from the Gaia DR2 (Gaia Collaboration et al., 2018) catalogue with spectroscopic parameters from the APOGEE (Abolfathi et al., 2018), LAMOST (Deng et al., 2012), RAVE (Steinmetz et al., 2006), GALAH (De Silva et al., 2015), Gaia-ESO (Gilmore et al., 2012), and SEGUE (Yanny et al., 2009) surveys.

- They use a sample of $\sim$3 million stars across a large range of Galactocentric radii ($\sim 3 - 15\,\mathrm{kpc}$).
- They use a Bayesian framework to characterize the probability distribution function of each star's distance, mass, and age, by fitting stellar isochrone models to their photometric, spectroscopic, and astrometric properties.
- Galactocentric positions and velocities are determined using distances and proper motions from Gaia DR2 combined with line of sight velocities from the spectroscopic surveys.
- A cut is made to select a subset of their 'best' giant and turnoff stars with [M/H]> -1, z$< 0.6\,\mathrm{kpc}$, and age uncertainty $< 45\%$. No further selection by chemical abundance is made.

- These stars are then binned by age (in 1.5 Gyr-wide bins between $[1, 11]$ Gyrs) and radius (in 1 kpc-wide bins between $[3, 15]$ kpc) to measure the vertical velocity dispersions.

- The sample does not distinguish between Galactic thin and thick disk components.

Note that uncertainties in the ages of young stars ($<\sim$ 2 Gyrs) in this sample are systematically larger than for older stars (which they note in their discussion). As we will see, this has noticeable effects on our star formation history predictions using SD18, since our model relies on scaling to present-day (ie. young) values. This aspect motivates our inclusion of a second source of data, M19, whose young stellar age determinations are more robust.

4.1.2 Mackereth+2019

Mackereth et al. (2019) (M19) provide stellar ages for 65,719 red giant branch (RGB) stars from cross-matching the APOGEE and Gaia DR2 surveys. Notably, they take a different approach from SD18 to measuring stellar ages.
RGB stars are typically difficult to estimate ages for using isochrone-fitting methods due to the overlap of isochrones at this stage in stellar evolution. Instead, they take advantage of the tight correlation between main sequence lifetime and stellar mass, as well as of the comparatively short RGB lifetime, and obtain age estimates based on estimating an RGB star's mass. Mass estimates for RGB stars can be derived from spectroscopic data, based on the ratio of carbon to nitrogen abundances ([C/N]). As a star evolves onto the RGB its convective envelope extends deeper into the interior, dredging up material enriched by the CNO cycle to the surface. Since the core [C/N] ratio and the depth of the convective boundary both depend on stellar mass, the surface [C/N] ratio after the first dredge-up can be used as a measure of that mass, and thus stellar age.

- M19 provide individual ages for 65,719 RGB stars spanning a range of $\sim$ 4 to $\sim$ 13 kpc in Galactocentric radius R, and $<\sim$ 2 kpc in height z. The smaller numbers of stars compared to SD18 mean that the extremes of this radial range are less well sampled, so in practice measurements are robust only between 6 and 11 kpc in radius.

- Galactocentric positions and velocities are determined using distances and proper motions from Gaia DR2 combined with line of sight velocities from APOGEE.

- Stellar ages are measured via a machine-learning approach, taking advantage of the correlation between the [C/N] ratio of an RGB star, its initial mass, and its main sequence lifetime. They use a Bayesian Convolutional Neural Network (BCNN) model, trained on a subset of 6,676 APOGEE stars with asteroseismic age determinations from the APOKASC-2 catalog (Pinsonneault et al., 2018). They input the entire normalized APOGEE spectra for each individual star (which contain molecular C and N features), rather than pre-determined stellar parameters from a pipeline, in order to capture more complex aspects of the relation between surface abundances and stellar age that might be missed in a more conventional approach. Median uncertainty of the ages are between ~ 30 to $\sim 35\%$, which corresponds to a median of ~ 1.26 Gyrs.

- Stars are binned by age (in 1.5 Gyr-wide bins between $[1, 10]$ Gyrs) and by [Fe/H] (in 0.2 dex-wide bins between $[-0.5, 0.5]$). A mean radius R_{Mean} is then measured for the binned stellar population.

- The Galactic thin and thick disks are separated chemically into α-poor and α-rich sequences, shown in their Figure 2. These are binned separately and plotted as filled circles (thin disk) and open circles (thick disk) in their Figure 5, which we reproduce in our Fig 4.1.

They note that their ages for older stars are probably systematically underestimated, such that ages above ~ 10 Gyrs are difficult to distinguish. In our case, however, we mostly concerned with stars formed in the past ~ 8 Gyrs, corresponding primarily to the thin disk, so this limitation does not significantly impact our analysis.

4.1.3 Age-Velocity Relations

Fig 4.1 shows the AVRs extracted from both sources. We have also included the radial velocity dispersions from Mackereth et al. (2019) since the ratio of vertical to radial dispersions is a useful measure of the contribution of different dynamical heating mechanisms in the Milky Way.
The observed velocity dispersions at fixed radii increase as a function of age across the

entire radial range. Both M19 and SD18 find that at all radii they are well described by power laws of the form $\sigma_z \sim t^{\beta}$ with index $\beta \sim 0.4$. This is qualitatively similar to what is seen in our simulations (Fig 3.10), where the trend of the AVRs with age are similar across all radii. This is an encouraging first observation for the applicability of our results.

Unlike what we see in our simulations, however, the observed AVRs at fixed age are not constant with radius. In the outer disk (R$>\sim$ 6 kpc) dispersions increase with increasing radius, and vice versa in the inner disk (R$<\sim$ 6 kpc) where dispersions increase with *decreasing* radius. This is visible in SD18 (left panel of Fig 4.1), where the greyscale lines indicate radial bins interior to those of M19, who examine only the outer disk. The origin of this trend in the inner disk and at young ages is currently unclear, and our simulated disk provides no obvious insight. SD18 suggest that it may be connected to the flaring of mono-age populations for a disk in equilibrium, or perhaps a selection effect favouring higher latitude stars in the outer disk. M19 further point out that the trends may be influenced by the Galactic bar, or that the disk may be perturbed by external interactions and thus not be in equilibrium. In our analysis we will focus primarily on the outer disk (R $>\sim$ 6 kpc), including the solar radius (R = 8 kpc), where our two sources of data overlap.

4.1.4 Scale Heights

Mackereth et al. (2017) (M17) measure the stellar density profiles in the disk of the Milky Way for stellar populations from the APOGEE survey binned by age and metallicity. They fit exponential scale heights as a function of radius to each binned population, allowing us to assign exponential scale heights to the corresponding velocity dispersion measurements from M19 and SD18.

Specifically:

- Stellar populations are binned by age (six 2 Gyr-wide bins between $[1, 13]$ Gyrs) and [Fe/H] (seven 0.1 dex-wide bins between [-0.6,0.2]).
- The same chemical thin/thick disk separation is made as in M19.
- The stellar density profiles for each binned population are modelled radially as a broken exponentials with scale lengths $h_{R,in}$ and $h_{R,out}$, and vertically as single exponentials with scale height z_h (h_z in their notation) that varies exponentially

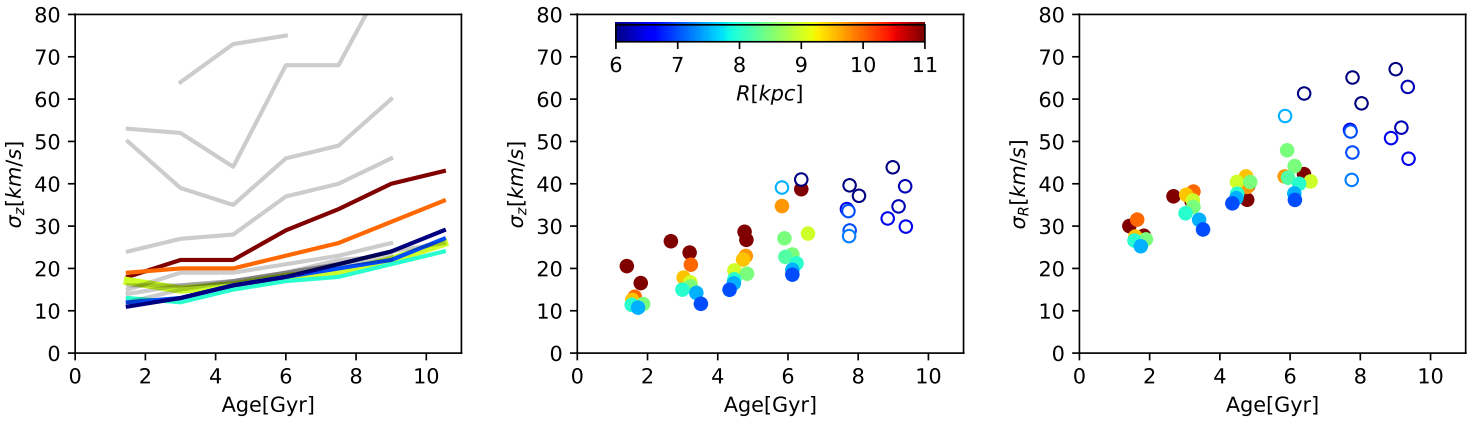

Figure 4.1: Reproduction of Sanders & Das (2018) (left) and Mackereth et al. (2019) (middle, right) AVRs from their Figures 10 and 5 respectively. Note that the colours in the Sanders & Das (2018) panel have been changed to match those of Mackereth et al. (2019). The range of inner radii not covered in M19 are shown in grey, where σ_z increases with decreasing radius in the inner disk (ie. the topmost grey line corresponds to SD18's innermost radial bin at 3 kpc). M19's data are separated into thin (filled circles) and thick (open circles) disk components.

with radius to produce a flared profile, of the form:

$$\nu_*(R, \phi, z) = \Sigma(R)\zeta(z|R) \tag{4.1}$$

where

$$ln\Sigma(R) \propto \begin{cases} -h_{R,in}^{-1}(R - R_0) & R \leq R_{Peak} \\ -h_{R,out}^{-1}(R - R_0) & R > R_{Peak} \end{cases} \tag{4.2}$$

and

$$ln\zeta(z|R) \propto h_z^{-1} exp(R_{flare}^{-1}[R - R_0])|z| - ln\, h_z(R) \tag{4.3}$$

with $R_0 = 8\,\mathrm{kpc}$ denoting the solar radius.

They present their best-fit scale height profiles as a function of radius for each binned population in their Figure 7, from which we determine the scale heights corresponding to the velocity dispersions measured in M19 and SD18.

For M19, which similarly bin by age and metallicity, we read off z_h for that population at the measured R_{Mean}. Note that M19's age bins are slightly smaller (1.5 Gyrs) than M17's (2 Gyrs), so we match the measurements by choosing the bin with the largest overlap. The metallicity bins, though of the same width, do not go as high in M17 (max [Fe/H] of 0.2) as in M19 (max [Fe/H] of 0.5). These higher metallicity bins correspond to the smaller R_{Mean} in M19 ($\sim 6 - 7\,\mathrm{kpc}$), so these will not be included in our $\sigma_z - z_{50}$ comparisons.

For SD18 we read off z_h for the age bin with the largest overlap, similar to what we do for M19, at the midpoint of each of SD18's radial bins. SD18 does *not* bin by metallicity, so we take the mean z_h of all M17's metallicity bins for each age and radius.

The exponential scale heights are then converted to half-mass scale heights z_{50} to make consistent comparisons with our analytic functions.

4.1.5 Milky Way Mass Profile Model

Finally, we need mass profiles and rotation curves of the Milky Way halo and disk to use as input into our analytical expressions for the self-gravitating (SG) and non-self-gravitating (NSG) relation between σ_z and z_{50} (equations 3.15 and 3.9). Specifically, the SG solution requires a vertical surface density profile for the disk ($\Sigma(z)$), and the

NSG solution requires the contribution of the dark matter halo to the rotation curve (V_{DM}).

For this we use the model of McMillan (2017) (McM17 hereafter). The model has six axisymmetric components: a dark matter halo, a stellar bulge, stellar thin and thick disks, and H1 and molecular (H2) gas disks.

They adopt an NFW profile for the halo:

$$\rho_h = \frac{\rho_{h,0}}{x(1+x)^2} \tag{4.4}$$

where $x = r/r_h$, with scale radius $r_h = 19.6kpc$, and $\rho_{h,0} = 0.00854 M_\odot pc^{-3}$.

The bulge is modelled as:

$$\rho_b = \frac{\rho_{b,0}}{(1+r'/r_0)^\alpha} \exp^{-(r'/r_{cut})^2} \tag{4.5}$$

where $\rho_{b,0} = 98.4 \mathrm{M}_\odot \mathrm{pc}^{-3}$, $r_0 = 0.075\,\mathrm{kpc}$, $\alpha = 1.8$, $r_{cut} = 2.1\,\mathrm{kpc}$, and $r' = \sqrt{R^2 + (z/q)^2}\,\mathrm{kpc}$ in cylindrical coordinates, with axis ratio $q = 0.5$. This is an axisymmetric profile, while the Galactic bulge is known to be triaxial. They note that this could cause inaccuracies in the inner few kpc of the Galaxy, but since SD18 and particularly M19 provide data mostly at larger radii this is not problematic for our analysis.

The thin and thick stellar disks are both modelled as a double exponential:

$$\rho_d(R,z) = \frac{\Sigma_0}{2z_d} \exp^{-\frac{|z|}{z_d} - \frac{R}{R_d}} \tag{4.6}$$

with scale heights $z_{d,thin} = 300\,\mathrm{pc}$ and $z_{d,thick} = 900\,\mathrm{pc}$, scale radii $R_{d,thin} = 2.50\,\mathrm{kpc}$ and $R_{d,thick} = 3.02\,\mathrm{kpc}$, and central densities $\Sigma_{0,thin} = 896\,\mathrm{M}_\odot\mathrm{pc}^{-2}$ and $\Sigma_{0,thick} = 183\,\mathrm{M}_\odot\mathrm{pc}^{-2}$.

The gas disks follow the density profile:

$$\rho_d(R,z) = \frac{\Sigma_0}{4z_d} \exp^{-\frac{R_m}{R} - \frac{R}{R_d}} sech^2(z/2z_d) \tag{4.7}$$

with scale heights $z_{d,H1} = 85\,\mathrm{pc}$ and $z_{d,H2} = 45\,\mathrm{pc}$, scale radii $R_{d,H1} = 7\,\mathrm{kpc}$ and $R_{d,H2} = 1.5\,\mathrm{kpc}$ of an exponential decline at larger radii, scale lengths $R_{m,H1} = 4\,\mathrm{kpc}$ and $R_{m,H2} = 12\,\mathrm{kpc}$ associated with a central hole, and central densities $\Sigma_{0,H1} = 53.1\,\mathrm{M}_\odot\mathrm{pc}^{-2}$ and $\Sigma_{0,H2} = 2180\,\mathrm{M}_\odot\mathrm{pc}^{-2}$.

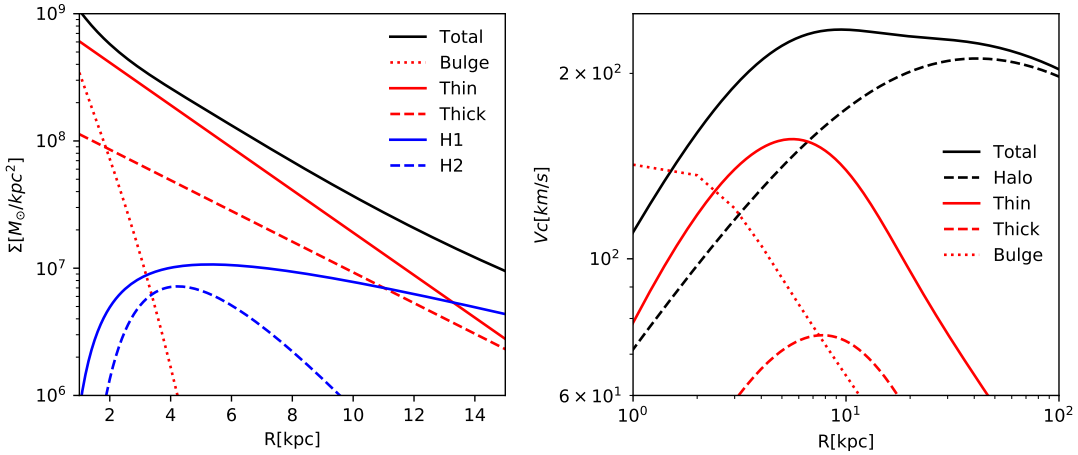

Figure 4.2: Milky Way model from McMillan (2017) used in the analysis. Left panel is surface density profiles for the Galactic disk, while the right panel is the rotation curve broken down by stellar and dark matter components.

The surface density profiles and circular velocities of all the McM17 model components are shown in Fig 4.2.

4.2 σ_z-z_{50} for the Milky Way

We first examine the observed $z_{50} - \sigma_z$ relations for the measured stellar populations of SD18 and M19, in comparison with the expected relations for an isothermal disk in vertical dynamical equilibrium derived in Section 3.3. This provides a check on the applicability of the assumptions of isothermality and dynamical equilibrium made in our model, so that for those data where the observed and expected relations are consistent, we can confidently apply our AVR-star formation history prediction later on.

Fig 4.3 shows the observed vertical velocity dispersion - scale height relations for SD18 and M19. The left and right panels show the velocity dispersions from SD18 (triangles) and M19 (circles) respectively, with corresponding scale heights from M17 for each stellar population. The lines on each panel show the expected relation between σ_z and z_{50} at a given radius for an isothermal disk in equilibrium, based on the combined self-gravitating and non-self-gravitating relations of Equations 3.15 and 3.9, and using the Milky Way mass profiles of McM17 to derive the necessary parameters

for each (the surface density $\Sigma(z)$ for SG and the contribution to the rotation curve from the dark matter halo V_{DM} for NSG). Points and lines are coloured by radius according to the legend in the right panel, matching those used earlier in Fig 4.1. The radii in SD18 that fall outside this range (4, 12, and 14 kpc) are added in greyscale according to the legend in the left panel. We do this in order to keep the same colour mapping used in M19 for consistency of comparison.

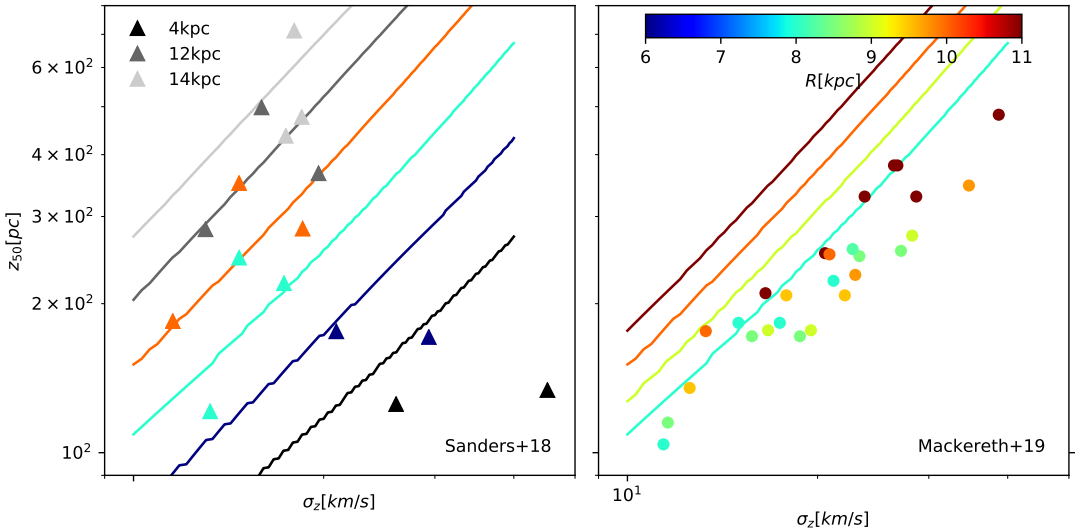

Figure 4.3: Observed MW velocity dispersions as in Fig 4.1, now plotted against half-mass heights for that population measured from M17. SD18 is shown on the left, while M19 is shown on the right. Points are coloured by radius, according to the colourbar in the right panel. The colours were chosen to match those used in M19, and so the radii outside this range in SD18 are shown in grey (see legend on left panel). The lines are the expected relation between σ_z and z_{50} at the same radii as the data, from Equations 3.15 and 3.9, and using the Milky Way density profiles of McM17. Lines in the right panel are for $R = 8$, 9, 10, 11 kpc, and lines in the left panel are for $R = 4$, 6, 8, 10, 12, 14 kpc, to match the respective ranges of the data.

We first examine M19 (right panel) since their data are binned similarly to M17, giving us more points for comparison than we will have for SD18 (left panel, which we describe next). Recall that each point of data here is a stellar population selected by age and metallicity, and coloured by the mean radius of the population. Note that we are showing only M19's thin disk populations, and that their thin disk populations with smaller mean radii ($<\sim 7$ kpc) are not included here since they correspond to higher metallicity bins than were measured in M17.

Immediately we see that there is an inconsistency between the observed values (points) and expected relations (lines) as a function of radius. Where the observations show minimal difference in scale height for a given velocity dispersion across the radial range, the expected relations predict a much greater change in scale height for a given velocity dispersion as a function of radius. The two converge around the solar radius at $R = 8\,\mathrm{kpc}$ (cyan). At face value, this suggests that the vertical acceleration due to gravity in the outer disk ($8 < R < 11\,\mathrm{kpc}$) does not change as much as a function of radius as expected in McM17's model, resulting in similar scale heights at fixed velocity dispersion across that radial range. We examine this further when comparing to the results for SD18.

In contrast, the observed monotonic increase in scale height with increasing velocity dispersion at a fixed radius *is* consistent with the expected trend, scaling approximately as $z_{50} \sim \sigma_z$, similar to what we saw in our simulated disk in Section 3.3. This is most easily seen where the observed points and lines nearly overlap at 8 kpc. Recall that the expected trend is constructed from the combined contributions to the vertical potential gradient from the dark matter halo and the baryonic disk, where the halo (scaling as $z_{50} \sim \sigma_z$ according to Equation 3.9) dominates at larger scale heights, while the self-gravity of the disk (scaling as $z_{50} \sim \sigma_z^2$ though modified to scale closer to $z_{50} \sim \sigma_z$ at small heights to account for the thickness of the disk according to Equation 3.15) dominates at small scale heights. This suggests that at any given radius in M19's radial range, the measured stellar populations are indeed isothermal and in vertical dynamical equilibrium, else the slope of the trends would not match what we expect given those conditions. *This is important*, as it provides confidence in our ability to apply our main result (the AVR-SFH relation) to M19's AVRs.

The left panel shows the same but for SD18, accounting for their larger radial range. Note that there are fewer data points per radius compared to M19. This is because SD18 do not subdivide their stellar populations by metallicity, resulting in fewer bins, and causing us to be limited by the size of the age bins in M17. Since SD18 do not make a thin/thick disk separation, we also exclude older age bins where the thick disk overlaps the thin disk in age, and so we are left with a maximum of three data points over an age range of $1 - 7\,\mathrm{Gyrs}$ at each radius.

Firstly, due to the small number of data points per radius, it is not possible to distinguish whether there is a monotonic trend at fixed radius $z_{50} \sim \sigma_z$ consistent with what is expected, as we did for M19. We can, however, see that the separation as

a function of radius is actually well-described by what we expect from the McM17 model, unlike what we see for M19 even over the same radial range. This is interesting, as it suggests that the inconsistency between radii of M19 compared to the expected in the right panel may not be due to a shortcoming of McM17's Milky Way model, but rather how M19's populations are binned and assigned a radius.

To show this difference between SD18 and M19 as a function of radius, we fit the expected $z_{50} - \sigma_z$ relation at each radius to the observed data for each. We do this by allowing McM17's total surface density parameter for the thin disk $\Sigma_{0,thin}$ from Equation 4.6 to vary while keeping all other parameters fixed. In effect, we are varying the magnitude of the self-gravitating component of the potential, to recover the total surface density gradient of the disk needed to match the scale heights at fixed velocity dispersion as a function of radius.
Note that we have varied $\Sigma_{0,thin}$ for simplicity, rather than other parameters such as the thin disk scale height $z_{d,thin}$ or the surface densities of the gaseous components $\Sigma_{0,H1}$ or $\Sigma_{0,H2}$. In practice, while allowing $z_{d,thin}$ to decrease in order to increase the 'effective' surface density felt by a thin stellar population can produce a similar effect to varying the total surface density directly, it essentially undoes the effect of the correction done to the SG solution to account for disk thickness (Section 3.3.2) by making the component more akin to a razor-thin disk. In doing so, the power law scaling of the relation becomes closer to $z_{50} \sim \sigma_z^2$ at small scale heights, and no longer matches the $z_{50} \sim \sigma_z^1$ trend of the data in that range. Similar effects occur when increasing the gas densities, since the H1 and H2 profiles have very thin scale heights. By varying $\Sigma_{0,thin}$ we can accurately fit both the magnitude of the relation as a function of radius as well as the $z_{50} - \sigma_z$ trend at fixed radius.
The best-fit value is determined using a simple chi-square minimization, the results of which we show in Fig 4.4, with M19 again in the right panel and SD18 in the left panel. Radial separations in M19 are now in line with the data, while SD18, which already matched well, changed very little. Importantly, the power law trend $z_{50} \sim \sigma_z^1$ of the relations still acceptably describes the observed data of M19.

The resulting best-fit total surface densities are shown compared to the base McM17 model in Fig 4.5, to provide a better visual comparison. Fitting M19 requires the total surface density of their measured outer disk range to be nearly flat, maintaining the same surface density as at $R = 8\,\mathrm{kpc}$, while SD18 follows the ex-

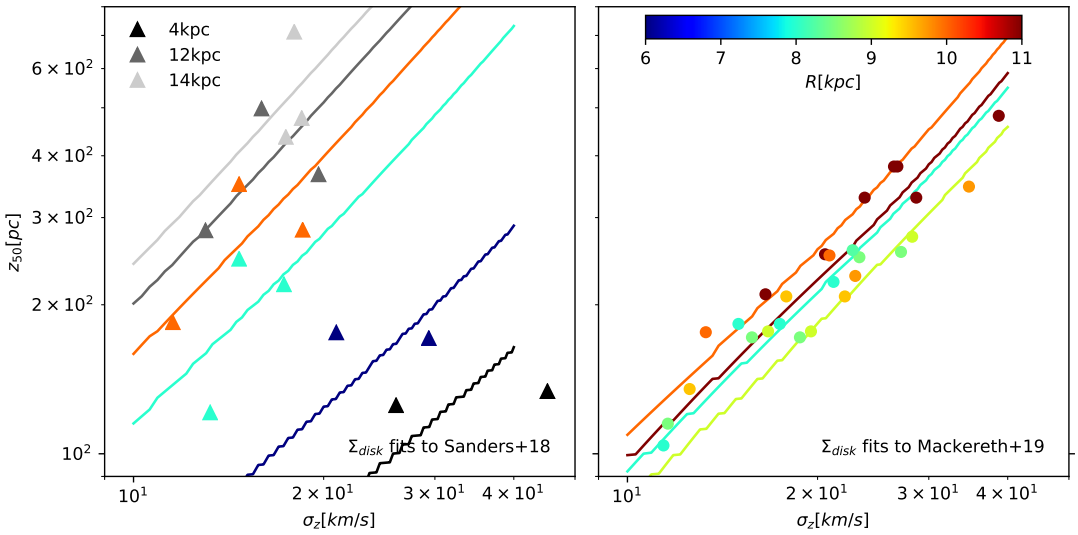

Figure 4.4: Same as in Fig 4.3, but with lines showing the best-fit relation at each radius.

pected radial gradient of McM17. This is puzzling, and is likely a consequence of the difference in binning between the two data sets. Since M19 do not bin directly by radius, but rather by age and metallicity and then estimate a mean radius for the sample, it is possible that their 'radius' does not correspond directly to the radii of SD18 and McM17, and that their effective radial range is smaller than otherwise indicated. Their measured populations could be in effect sampling the potential closer to 8 kpc than their measured R_{mean} would suggest. The fact that SD18, who *do* bin explicitly by radius, are by contrast consistent with McM17 over the same radial range ($8 - 11$ kpc), would seem to support this interpretation.

We draw two main conclusions from this section. First, since the $z_{50} - \sigma_z$ relations based on McM17's Milky Way model are well-matched as a function of radius by SD18 (who bin populations directly by radius), but not by M19 (who measure a population's 'mean radius') beyond the solar radius at $R = 8$ kpc, we must be careful when drawing conclusions from M19's radial trends in the outer disk. However, given that M19's solar radius was consistent with both SD18 and McM17, we can more confidently use their results at 8 kpc.

Second, and most importantly, the consistency of M19's $z_{50} - \sigma_z$ trends *at fixed radius* with our expected $z_{50} \sim \sigma_z^1$ trends for an isothermal disk in vertical dynamical equilibrium gives us confidence that the conditions necessary to apply our AVR-SFH

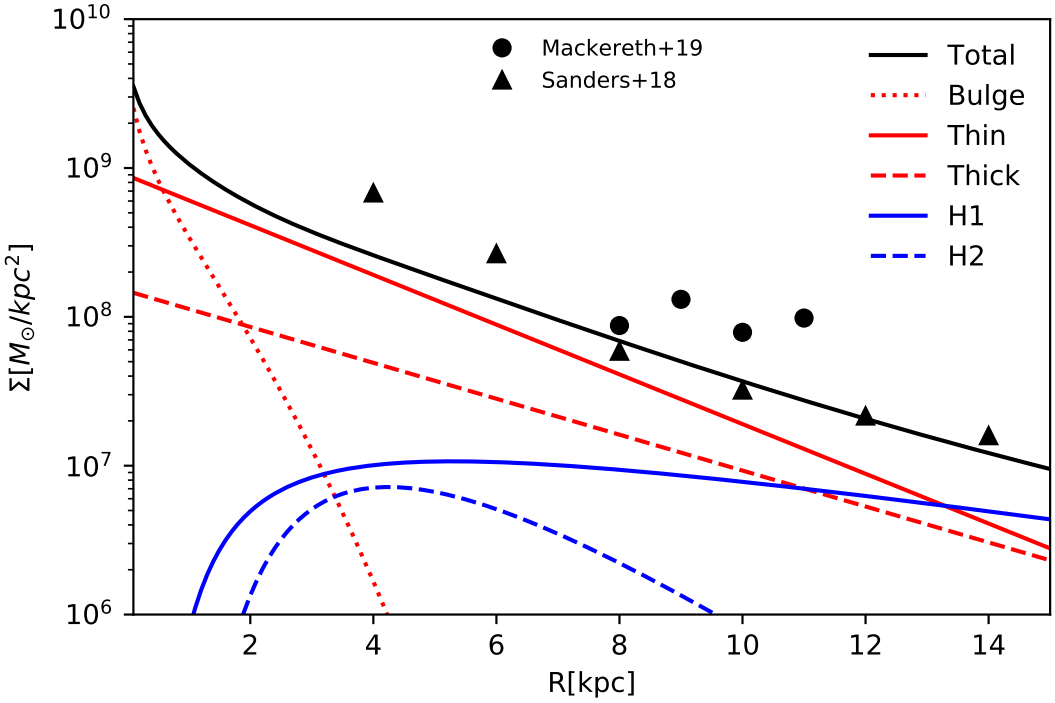

Figure 4.5: Expected surface densities as a function of radius from fitting predicted σ_z-z_{50} relations to observations shown in Fig 4.4. Lines are the surface density profiles from the McM17 MW model. Black points show the total surface density using the fitted results from Fig 4.4 for M19 (circles) and SD18 (triangles).

relation to this observed data are met. In particular, we are most confident in M19's AVR at 8 kpc given the first conclusion, and since SD18 did not have enough data to confidently test its $z_{50} - \sigma_z$ relations in the same way, we will focus on the results of M19 for the solar neighbourhood when applying our main result in the following section.

4.3 Applying AVR - SFH Relation to Milky Way

In this section we apply our main result, the ability to predict a star formation history (SFH) based on a local age-velocity dispersion relation (AVR), to the observed AVRs of the Milky Way presented above. Following the conclusions of the previous section, we will be focusing initially on the AVR and SFH at the solar radius. By comparing our result to other predicted SFHs for the solar radius from the literature, we can assess the role of upside-down formation in setting the observed vertical structure of the disk of the Milky Way.

To recover a predicted star formation history we simply apply the fitted power-law relation shown in Fig 3.11 to the observed AVRs. This returns a star formation rate as a function of lookback time normalized to the present-day rate at the measured radius, which can be converted to physical units if the present-day rate is known. This predicted star formation history assumes that the same conditions that make it valid in our simulation are also true of the Milky Way: that the local potential has not significantly changed over the measured time period, and that the AVR is set by upside-down formation from an isothermal gaseous disk in HSE and is not significantly affected by vertical heating. Though there is good evidence that vertical heating may have a role in the Milky Way, by comparing our result to other predicted star formation histories for the Milky Way from the literature we aim to provide a constraint on our feedback-regulated upside-down formation scenario.
Unfortunately the local SFH of the solar neighbourhood is still not robustly known. There have been a variety of approaches taken in the literature to measure or model the local SFH, and though these provide some constraints they have still not fully converged.

4.3.1 SFH of the Solar Neighbourhood from the Literature

We describe here a sample of recent results from the literature for comparison to our own prediction, all of which are reproduced together in the middle panel of Fig 4.6 along with our own result.

Just and Jahreiß 2010

Just & Jahreiß (2010) (JJ10 hereafter) develop an evolutionary disc model of the solar cylinder described by a local star formation history, a local age-velocity relation, and a local age-metallicity relation. The disc is modelled as a set of mono-age stellar subpopulations in vertical dynamical equilibrium within a potential generated by the stellar, gaseous, and dark matter components of the Galaxy. The star formation history and age-velocity relation are implemented as smooth analytic functions which, along with a monotonically increasing age-metallicity relation to model local chemical enrichment, describe for each mono-age population a vertical density distribution, vertical velocity dispersion, and metallicity.

It must be noted that this disc model is fit to local data and does not account for significant amounts of radial mixing. In this context, it is perhaps more correct to interpret their 'star formation history' as a current age distribution rather than a formation rate over time.
The model is fit to a volume complete sample of main sequence stars in the solar neighbourhood, largely defined by the Hipparcos catalog, and combined with spectroscopic measurements to determine velocity distribution functions (see their Section 3). They obtain best-fit parameters for the star formation history and age-velocity relation simultaneously and test different parametrizations of the two together.
We reproduce for comparison their model A, which is their favoured model, as well as their model B, which also yielded good fits to their data. While they found good convergence in their age-velocity relations, the star formation histories were only weakly constrained. Model A corresponds with the upper bound of their allowed star formation history variation, peaking at $\sim$ 10Gyrs lookback and decreasing by roughly a factor of 4 to the present-day.
Note that they also test a model C, which has a constant star formation rate over all ages and provides similarly acceptable fits as their model B. This model overlaps with some of our other histories from the literature (described below), and so it is not included explicitly for visual clarity.

Kubryk et al 2015

Kubryk et al. (2015) (K15 hereafter) develop a chemical evolution model of the Milky Way following an 'independent ring' approach, in which the Milky Way is modelled as a series of radial annuli, each of which undergoes its own 1D chemical evolution. The basis of this method is a parametrized gas infall rate as a function of radius and time (see eg. Chiappini et al. (1997)). Star formation rates in each annulus are in turn calculated based on the local gas density, and the supernovae resulting from these stars drive local chemical enrichment. The model parameters are then tuned to satisfy observational constraints, such as total stellar mass, total gas mass, radial stellar and gas density gradients, present-day star formation rates and gas infall rates, radial chemical gradients (eg. of [Fe/H] and [O/H]), and local abundance-age relations. This approach can thus provide (among other results) predicted star formation rates in the galaxy as a function of time and radius.

K15 make a number of additions to this base approach. Notably, they include parametrizations for the effect of radial migration of stars, as well as radial gas flows. This allows neighbouring annuli to affect each other's chemical evolution, where they would otherwise evolve completely independently. For the solar radius this acts to flatten the local star formation history, since older stars that are comparatively metal-rich are no longer entirely dependent on chemical enrichment from in-situ star formation, and can instead have either migrated from the more metal-rich inner disk or have formed from gas that was enriched in the inner disk and flowed outwards.
We include for comparison the star formation history of the 8 kpc annulus of their base model (from their Figure 3).

Toyouchi et al 2018

Toyouchi & Chiba (2018) (T18 hereafter) also develop a chemical evolution model using the independent ring approach. They use the same fundamental approach as K15, and though there are some differences in implementation (eg. T18 include a 'break radius' as an added free parameter in their gas infall model), they account for the same physical processes. Notably, they additionally include a parametrization for the re-accretion of gas outflows back onto the disc, which are preferentially ejected from the inner disk to settle on the outer disc, and tune their model to recover the radial dependence of the disc's metallicity distribution functions.
This provides another source for the movement of enriched materials from the inner disc to the outer disc, and their predicted star formation rates in the outer disc are further depressed at early times as a result. We include for comparison their predicted star formation rate over time at the solar radius from their Figure 6.

Snaith et al 2015

Finally, Snaith et al. (2015) (S15 hereafter) develop a chemical evolution model with a slightly different approach. The disc is divided into an inner disc ($R< 7-8$kpc) that behaves like a closed-box system, and an outer disc ($R> 9-10$kpc) defined by a single large gas accretion event at early times. Rather than assuming a prescription for star formation based on gas density, they recover a star formation history directly by fitting to observed chemical abundance trends as a function of age, essentially working backwards from the present-day rather than forwards like K15 and T18. This returns star formation histories that are measured discretely rather than as a

smooth parametrized function. Their driving concept is that the thick disc forms early on from a turbulent, well-mixed inner disc, which then transitions to a more typical inside-out process along with the outer disc to form the thin disc. At the solar radius this means that at the onset of thin disc formation there is considerable chemical enrichment already available, both due to local star formation as well as stellar migration and gas flows, which allows for flatter recent star formation histories similar to K15 and T18.
We use for comparison their fitted outer disc star formation history (their Figure 9), which they consider to be appropriate for the solar neighbourhood.

4.3.2 Predicted SFH

Recall that our AVR-SFH relation derived in Section 3.4 relates the local surface density of star formation as a function of lookback time to the change in the vertical velocity dispersion as a function of stellar age, approximately as a power law of the form $\Sigma_{SFR} \sim \sigma_z^n$ with index $n = 1.82$. Thus, if the velocity dispersion at a given radius increases with age, then the star formation rate at that radius will increase with lookback time accordingly.
We have seen that the observed AVRs of both SD18 and M19, shown in Fig 4.1, increase with age over their entire radial range ($3 - 15\,\mathrm{kpc}$ and $6 - 11\,\mathrm{kpc}$ respectively) and scale similarly at all radii. We therefore expect that our relation will predict star formation histories in the disk that increase with lookback time at all radii, and that these local star formation histories will scale similarly at every radius.

We show the result for the solar radius explicitly in Fig 4.6. The left panel reproduces the AVRs for the solar neighbourhood ($R = 8\,\mathrm{kpc}$) from SD18 (triangles) and M19 (circles), extracted from Fig 4.1. For our comparison we will focus in particular on the AVR of M19, for two reasons. First, based on the analysis of the $z_{50} - \sigma_z$ relations from the previous section (Section 4.2) we are most confident that their stellar populations at this radius are isothermal and in dynamical equilibrium. Second, SD18's youngest ages have large associated uncertainties, causing their AVRs flatten out significantly in their youngest age bins. Since our SFH prediction relies on scaling the youngest stars, this artificially flattens the predicted SFH. For these reasons we will be using the predicted SFH from M19's AVR for comparison and discussion, though we include SD18 on the middle and right panels for completeness.

The middle panel shows our main result: the predicted SFHs obtained by applying our relation to the AVRs of the left panel, compared to the SFHs for the solar radius from the literature described earlier. All SFHs have been normalized to their present-day values.

Only JJ10's models A and B increase with age like our predicted SFHs. Of these, model A matches our predicted SFH fairly well, increasing by about a factor of 3 up to an age of 6 Gyrs. By contrast, the other SFHs do *not* increase with age: K15 and S15 are flat over the same age range, and T18 *decreases* with age. These models seem inconsistent with our prediction, since in our scenario a constant (or decreasing) star formation rate with age has no means of producing an increasing AVR as is observed. Thus it appears that our predicted history is consistent with the upper range of those from the literature, though this range is large and not well agreed upon.

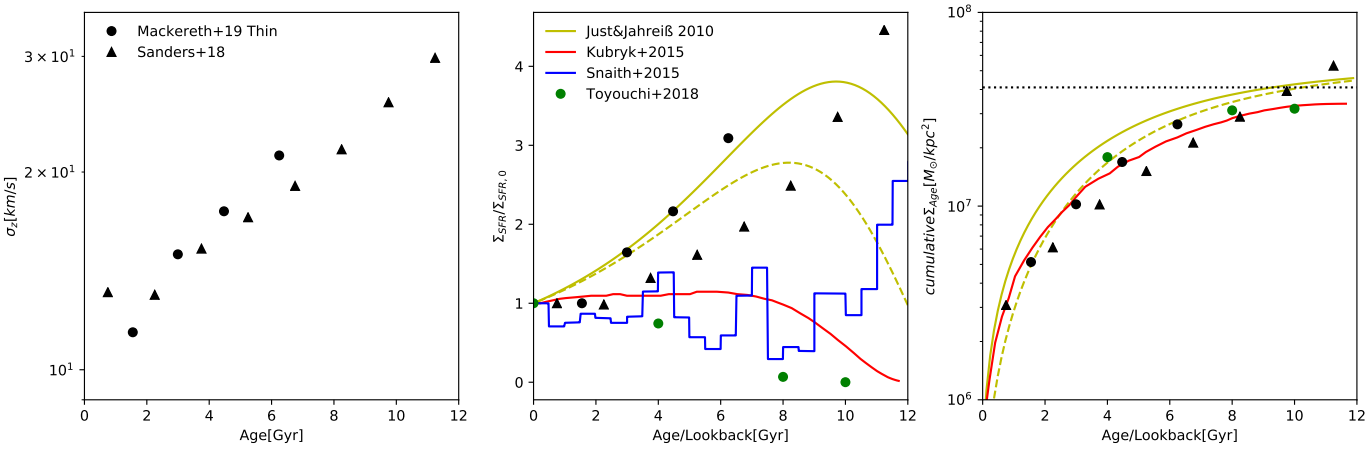

Figure 4.6: Left: Solar neighbourhood (8kpc) AVR for Milky Way using Mackereth et al. (2019) (circles) and Sanders & Das (2018) (triangles). Middle: Predicted star formation history for the solar neighbourhood based on applying our velocity dispersion-star formation relation to the local AVR's in the left panel, compared to local star formation histories from the literature. Just & Jahreiß (2010) lines are their models A (solid) and B (dashed), and the Snaith et al. (2015) is their outer disk history. All SFHs are normalized to their z=0 star formation rate. Right: Same data and models as middle panel, integrated to show cumulative age distributions (as in Fig 3.12). Dotted horizontal line is the total surface density of the McM17 model's thin disk component at the solar radius.

Finally, in the right panel we show the cumulative surface density of stars as a

function of age for each history from the middle panel, in the same way as we did for the simulation in Fig 3.12. This is to check whether a given star formation history recovers the local stellar age distribution (or, cumulatively, the surface density of the stellar disk). These are in physical units, not normalised to z=0, so for our result we require an initial star formation rate to scale from. We use the star formation rate at the solar radius from Blitz & Rosolowsky (2006) (their Figure 5), who provide a current star formation gradient for the Milky Way based on an H2-pressure relation applied to observed molecular gas densities. We do not include the S15 history in this panel, since in their paper it is not presented in physical units. Each of the other sources provide their histories in physical units. We also include on the panel a horizontal line indicating the total thin disk surface density at 8kpc of the McM17 model as a point of reference.
Extrapolating our predicted surface density matches McM17's thin disk in the $8-10$Gyr range. More importantly, it falls within the range of the other models, which expect cumulative surface densities at the 8 Gyr age mark (the approximate age of the thin disk) between $2.5-3.5\times10^{7}\,\mathrm{M_{\odot}\,kpc^{-2}}$.

Overall our results do not provide a clear constraint on an upside-down formation scenario for the disk of the Milky Way. This stems from the fact that our metric for comparison is a predicted local star formation history, which is neither directly measurable nor fully agreed on in the literature. We have shown in the middle panel of Fig 4.6 that possible SFHs at the solar radius range from one increasing with age similar to our result (JJ10 model A), to flat recent histories (K15 and S15), to decreasing rates with age (T18). Since our prediction is consistent with the upper bound of this range, and also recovers a local stellar surface density that is consistent with the other approaches, we can at least conclude that upside-down formation is not ruled out based on this comparison alone.

4.4 Velocity Dispersion Ratio

In this section we make a qualitative comparison between the ratios of vertical to radial velocity dispersions of our simulated disk versus the observed ratios in the Milky Way. The dispersion ratio provides a useful measure of the contribution of vertical heating mechanisms in the disk (introduced in Section 1.5.3). Since the result of our

predicted star formation history in the previous section was inconclusive, the aim of this comparison is to provide additional constraints on an upside-down formation scenario for the Milky Way.

Fig 4.7 shows the dispersion ratios of our simulated disk (left panel) and the data from M19 (right panel).
Recall that for our simulation (left panel) we bin stars by age and radius, and then measure the velocity dispersion of the binned population. Here we are simply taking the ratio of the vertical dispersion of these stellar populations (shown previously in Fig 3.10) to the radial dispersion. Each radius is coloured according to the legend in the left panel. Note that here we show only the running medians of the age bins for each radial bin for visual clarity. As before, we distinguish between stellar properties as a function of age at the end of disk formation (Stars(t_4), solid lines) and properties of the stars of the same age at the time of their formation (Young stars(t), dotted lines).
As we see from the young stars over time (dotted), once the quiescent disk formation period starts at 8Gyrs the ratios at formation are relatively constant with time, holding at a value of $\sigma_z/\sigma_R \sim 0.8 - 0.9$. There is little variation as a function of radius, because in our simulation feedback is implemented isotropically, where energy is injected into surrounding gas particles with no directional preference, and the simulation uses an equation of state for the gas that leads to large isotropic pressures (see Section 2.1.5). Thus, in our gradually thinning disk regulated by feedback it is perhaps not surprising that the vertical and radial dispersions of newly formed stars scale similarly as a function of time.

The values as a function of age at t_4 (solid) are slightly different. We can see that the dispersion ratios decrease slightly after formation, and since we have already seen from Fig 3.5 that σ_z does *not* change, this can only be due to small increases in σ_R over time. We expect that the simulated stellar disk should experience some amount of radial heating from overdensity features in the disk, so this is not surprising. Overall, although the dispersion ratio as a function of age decreases slightly, especially at smaller radii, it remains relatively constant around values of $0.7 - 0.8$.

The observed ratios (right panel) are again from Mackereth et al. (2019) (M19), where both the vertical and radial dispersions are shown in Fig 4.1, and we simply

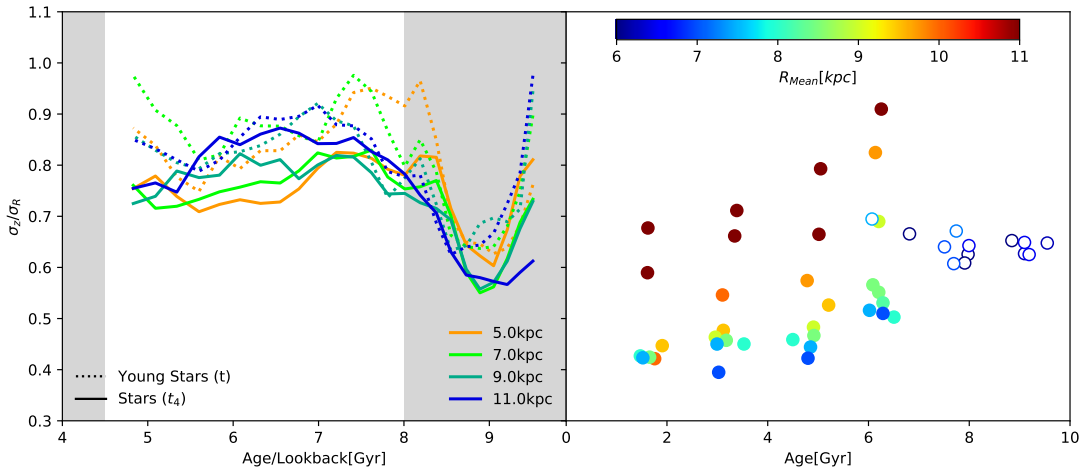

Figure 4.7: Ratio of vertical over radial velocity dispersions. Left: Young stars over time (dotted) and stars as a function of age at t_4 (solid) in the simulation. Right: Milky Way from Mackereth et al. (2019), coloured by radius and separated into thin (filled circles) and thick (open circles) disks, as in Fig 4.1.

plot the ratio of these values (as they do in their Figure 7). Note that the colour schemes between the left and right panels are deliberately different, because we want to compare radial trends within each rather than specific radii between the simulation and observations.

The observed thin disk ratios differ from our simulation results, particularly in the outer disk. At all radii the ratios increase with age, with inner radii in the range of $\sim 0.4 - 0.5$, while their outer radius increases from $\sim 0.7 - 0.9$. M19 describe this trend with age in their lower radii ($< 10\,\mathrm{kpc}$) as consistent with being due to vertical heating from scattering off giant molecular clouds (GMCs) combined with radial heating from disk instabilities, based on the work of Aumer et al. (2016a). As star formation rates in the disk decrease, corresponding to a decrease in GMCs, newly-formed stellar populations experience less vertical heating than older populations, and so saturate to a lower σ_z/σ_R. The resulting trend with age in the $\sim 0.4 - 0.5$ range matches the observations quite well.

However, this does not account for the observed ratios at 11 kpc. At $\sim 0.7 - 0.9$ these are greater than expected even for the case where GMC heating remains constant over time, which expects values to reach a maximum at ~ 0.6. M19 do not provide any definitive explanation for why this might be, though they again suggest that the outer disk may have been affected by perturbations from external sources.

The dispersion ratios in our simulated galaxy are clearly too high compared to what is observed in the Milky Way. We have seen that our simulated disks tend to be too thick (ie. our simulation has $z_{50} \sim 0.5 - 1.0\,\mathrm{kpc}$ at our half-mass radius (Fig 3.8) compared to the observed $z_{50} \sim 0.1 - 0.3\,\mathrm{kpc}$ around R_{sun} (Fig 4.3)), so the difference in the ratio is likely due to a higher σ_z rather than a lower σ_R. This may stem from a combination of the EAGLE equation of state and a low density threshold for star formation causing stellar populations to form with artificially high vertical velocity dispersions.

Overall our feedback-regulated upside-down formation in the simulated disk does not easily explain the observed dispersion ratios. There is no obvious means for our simulated disk to produce the observed range of values, nor the trend of increasing ratio with increasing age seen at all observed radii. Our model expects the ratios at formation to be constant over time, and for the vertical velocity dispersions to be preserved. Reproducing the observed trend would require younger populations to experience more radial heating than older populations, whereas we might naively expect the inverse: that older populations have experienced greater radial heating over time.
Note that this does not necessarily discount this scenario entirely, but rather how it arises in the EAGLE code used in our simulations. It is possible that a similar scenario achieved with a different implementation could more closely match the Milky Way. The inclusion of further comparisons to other simulations (eg. Auriga (Grand et al., 2017), FIRE (Hopkins et al., 2014)) is an obvious next step beyond this work.

4.5 Chapter Summary

In this chapter we have applied our model from Chapter 3 to observations of the stellar disk of the Milky Way. The observed data are sourced from Mackereth et al. (2019) (M19) and Sanders & Das (2018) (SD18), which both provide catalogs of individual stellar age determinations and 6D phase space measurements from cross-matches of photometric and spectroscopic surveys that cover a wide range of galacto-centric radii.
We test the observed $\sigma_z - z_{50}$ relations at fixed radii against predicted relations using our results from Section 3.3, and find that at minimum the results for the solar neighbourhood are consistent enough to be confident proceeding with applying our

AVR-SFH model.
The predicted star formation history for the solar neighbourhood is within the range of predictions from the literature, though they themselves are not well converged, leaving the validity of our feedback-regulated upside-down formation scenario in the Milky Way unclear. The resulting predicted cumulative age distribution is also consistent with the local stellar surface density.
A final comparison of σ_z/σ_R ratios of the simulation versus the Milky Way indicate that our scenario, as implemented with the EAGLE code, cannot easily explain the observations, where the simulation's values are both larger and more constant over time than what is observed. Further comparison with other simulations that produce similar upside-down formation would better clarify the possible role of this process in the Milky Way.

4.6 Thesis Summary

- We make use of the APOSTLE simulation suite to understand how vertical structure (eg. the age-velocity dispersion relation) arises in a galactic disk. The disk components of the simulation's set of Milky Way analogue galaxies are characterized in order to select one for detailed analysis. We choose one (V4G0) that is disk-dominated and has a long period of quiescent disk formation, with a minimum of external interactions.

- We find that vertical structure in the simulated disk arises from a process of upside-down formation, where the stellar disk forms from a gradually thinning gaseous disk that is flared at all times, whose rate of thinning is regulated by star-formation induced feedback. A lack of sources of vertical heating in the simulation allow the vertical structure of the young stellar disk as a function of time to be preserved up to the end of the quiescent period, and are identically traced by the final stellar disk as a function of age.

- We derive a physical model of the vertical disk structure, in which an isothermal gaseous disk is in quasi-hydrostatic equilibrium, with the restoring force component dominated by kinetic pressure from bulk motion of the gas rather than thermal pressure. This model accurately describes the properties of the simulated disk at all times throughout the quiescent period of disk formation.

- The relation between velocity dispersion and current star formation rate as a function of time at a fixed radius is found to be well-approximated by a power law of the form $\Sigma_{SFR} \sim \sigma_z^n$, with a best fit value of $n = 1.82$. This provides a simple parametrization of how the complex and non-linear interactions between radiative cooling, star formation, and feedback, implemented numerically in the simulation, produce the resulting vertical structure. This enables us to predict the star formation history in the simulated disk based only on the final age-velocity dispersion relation.

- We apply this model to recent observations of the age-velocity relations of the Milky Way to obtain predictions for the local star formation history at a given radius, in order to test whether the upside-down formation scenario of our simulation is consistent with the observed Galaxy. We find that our predicted history is not inconsistent with the range of possible histories for the solar neighbourhood, and its resulting cumulative surface density in the solar neighbourhood is also consistent. However, the wide range of allowed histories from the literature otherwise render the comparison inconclusive.

- Finally, we examine the ratio of vertical to radial velocity dispersions of stellar populations in the Milky Way and make a qualitative comparison with our feedback-regulated upside-down scenario. We find no *direct* indication that our scenario is able to produce either the magnitude of the observed ratios, nor their trends with age, both of which are more readily explained by vertical heating models in the literature. However, the possibility remains that a simulation which produces similar behaviour, but with different implementations of physical processes such as stellar feedback, may more closely match what we observe in the Milky Way. Further comparisons with other simulations suites in the literature are a clear next step for future work.

4.7 Final Thoughts

The stated goal of this work has been to study the formation of vertical disk structure in our simulated galaxies, and apply the results to the Milky Way in order to better constrain the roles of formation versus heating in the Galactic disk. We have derived a model for feedback-regulated upside-down formation as the primary driver of vertical structure and compared it to the Milky Way, but the available data are currently

not enough to neither confirm nor rule out this model. Although our main metric for comparison, the local star formation history, is consistent with the range of possible histories from the literature, we are limited by the fact that there is not widespread agreement on those, even for the solar neighbourhood. Furthermore, our qualitative comparison of the velocity dispersion ratios suggests that our model may not explain the observations as cleanly as does vertical heating, with the possible exception of the outer disk. We suggest this may be due to our simulated disk forming stellar populations with artificially high vertical velocity dispersions, due to a combination of the EAGLE equation of state and a low density threshold for star formation. This will improve with future work and other simulation codes; indeed, the recently published Bird et al. (2021) examine a simulated disk based the GASOLINE code (Wadsley et al., 2004), whose disk forms upside down but is dynamically colder than ours, forming with much smaller velocity dispersions at birth. Their resulting AVR compares very favourably to the Milky Way (though it is worth noting that in their case dynamical heating and radial migration play a comparatively larger role, and feedback less so, than in ours, so the comparison with our model is not so straightforward).

Overall, the picture remains somewhat unclear. The opinion of this authour is that our model for feedback-regulated upside-down formation as the origin of vertical structure in the Milky Way (at least, as arises in our simulation based on the EAGLE code) does not seem favourable, given both the recent direction towards flatter star formation histories in the literature compared to ours (Section 4.3), and that our ability to reproduce the observed velocity dispersion ratios is largely speculative (Section 4.4). Further clarification of our results would be possible if progress is made on the local star formation history. Additionally, applying a chemical evolution model of our own, in which we fix the star formation rates based on our AVR-SFH relation, and test the inclusion of migration and radial gas flows as in K15 and T18, may also provide better constraints on our proposed SFH. Finally, including other simulation suites in our analysis (eg. Auriga (Grand et al., 2017), FIRE (Hopkins et al., 2014)), which have different implementations of key physical processes than ours, would provide a broader basis to compare with observations. Unfortunately these are beyond the scope of this thesis, and must be left for later research.

Appendix A

Other Disk Galaxies In Apostle

A.1 Other Disk Galaxy Histories

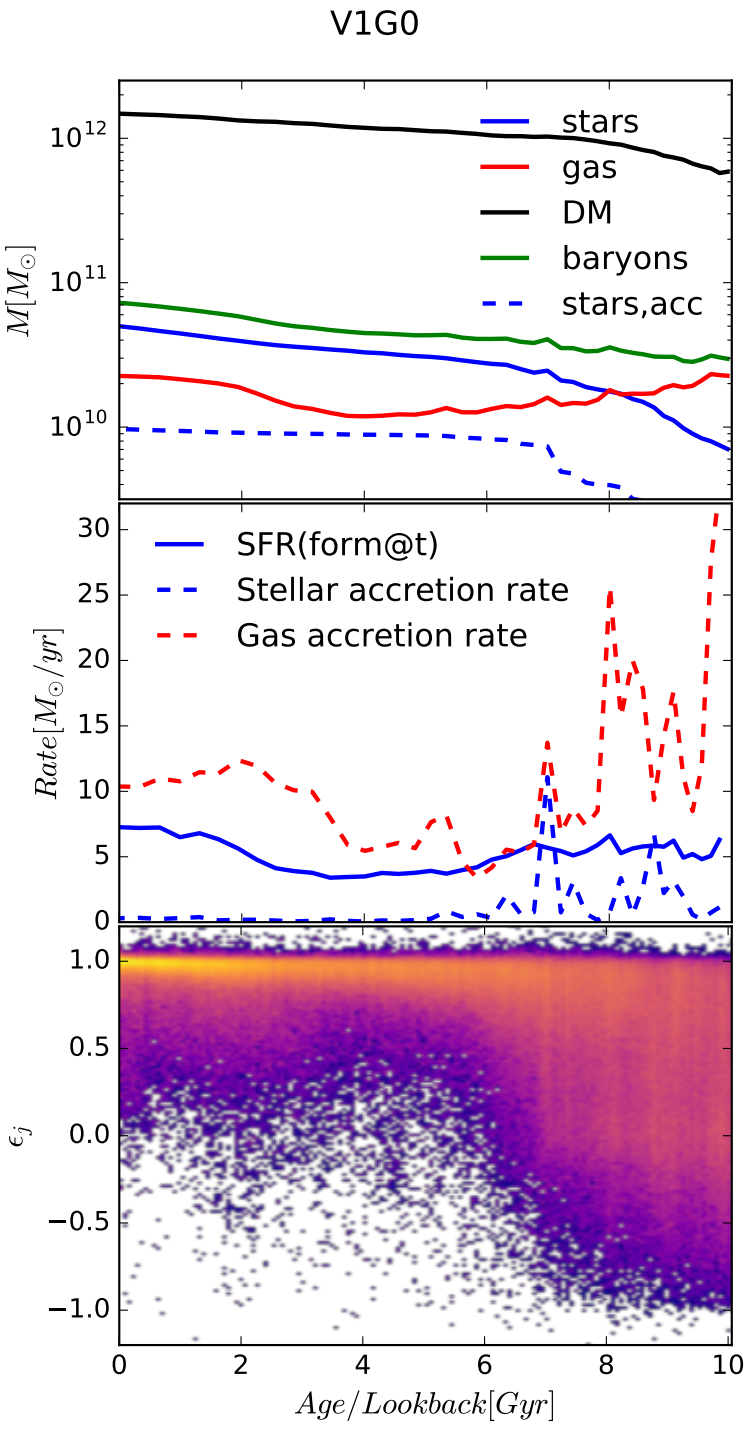

Figure A.1: As in Fig 2.5, for V1G0

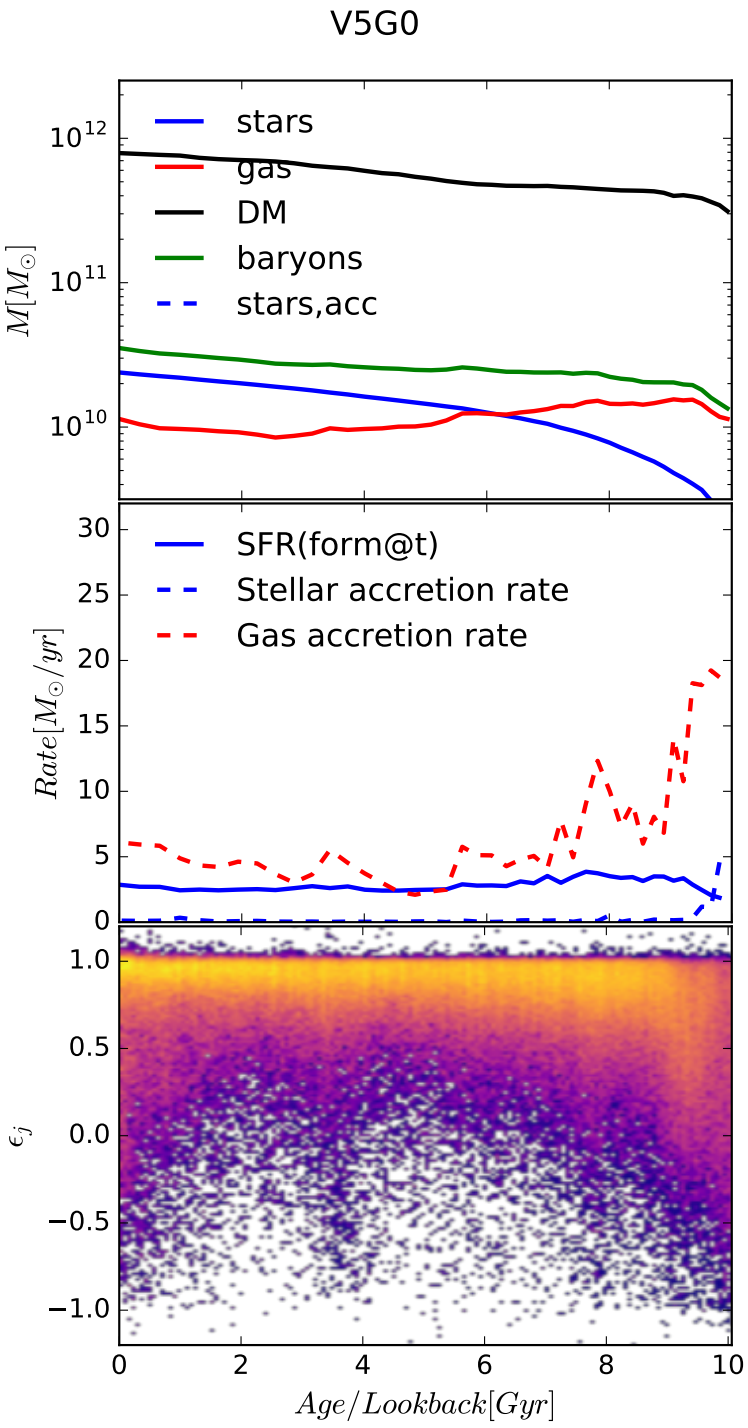

Figure A.2: As in Fig 2.5, for V5G0

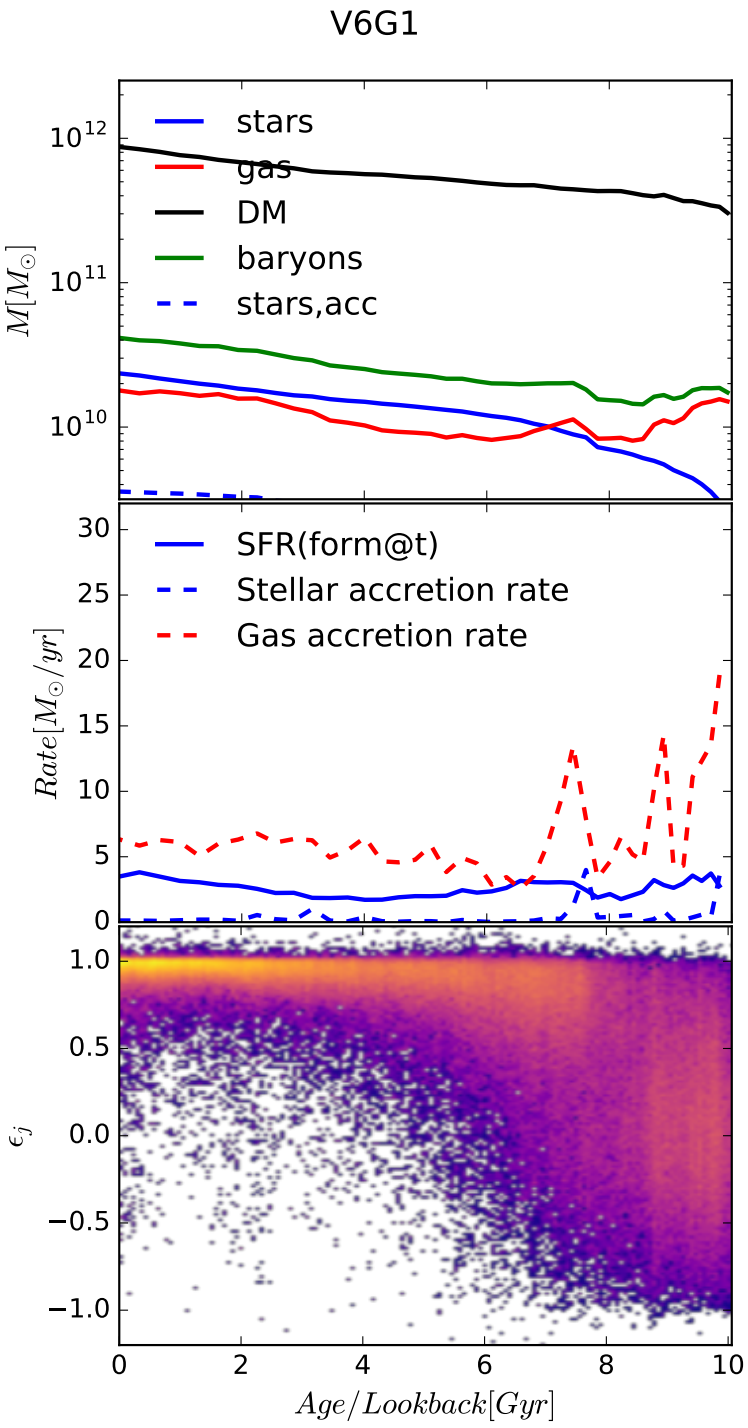

Figure A.3: As in Fig 2.5, for V6G1

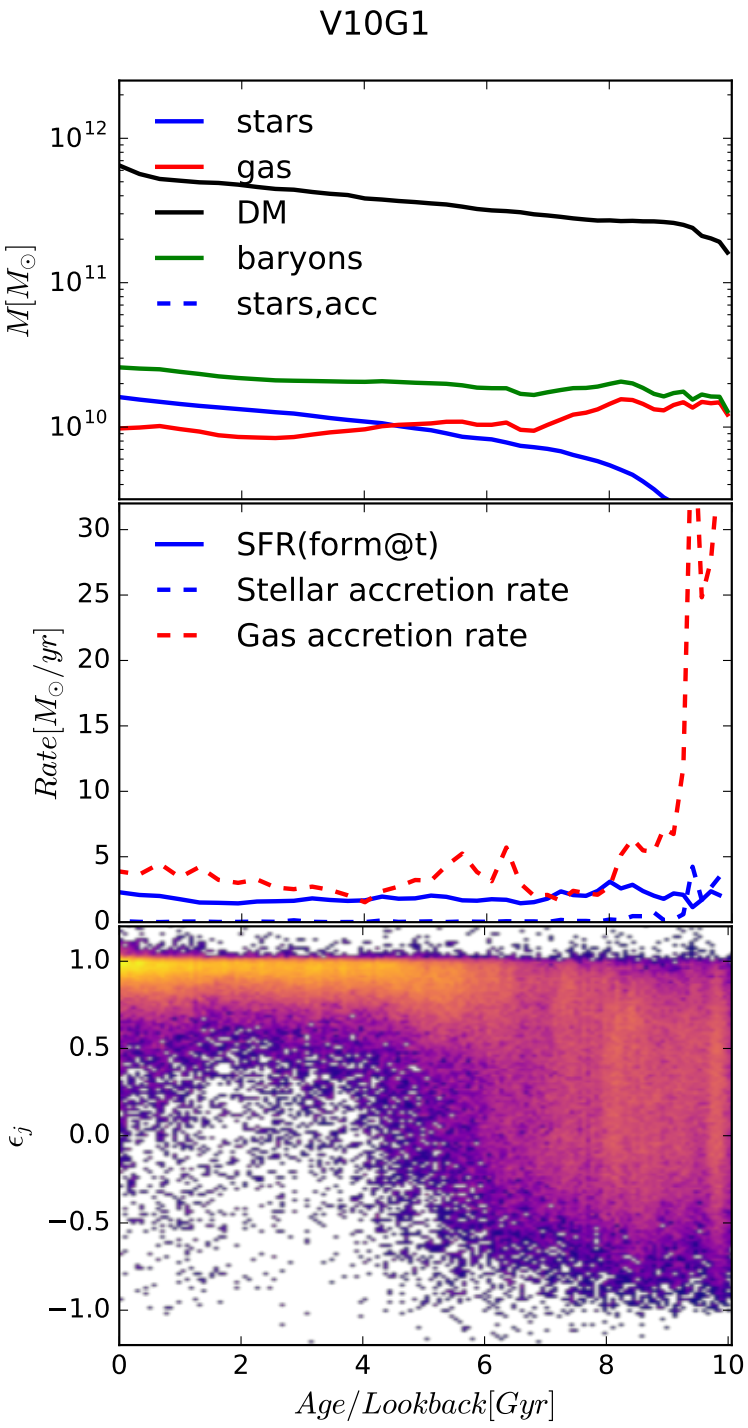

Figure A.4: As in Fig 2.5, for V10G1

Bibliography

Abolfathi B., et al., 2018, Astrophysical Journal, Supplement, 235, 42

Aumer M., Binney J., Schönrich R., 2016a, MNRAS, 459, 3326

Aumer M., Binney J., Schönrich R., 2016b, MNRAS, 462, 1697

Benítez-Llambay A., Navarro J. F., Frenk C. S., Ludlow A. D., 2018, MNRAS, 473, 1019

Benson A. J., 2010, Physical Reports, 495, 33

Benson A. J., Bower R. G., Frenk C. S., Lacey C. G., Baugh C. M., Cole S., 2003, ApJ, 599, 38

Bergemann M., et al., 2014, A&A, 565, A89

Binney J., Tremaine S., 1987, Galactic dynamics. Princeton, NJ, Princeton University Press

Bird J. C., Kazantzidis S., Weinberg D. H., 2012, MNRAS, 420, 913

Bird J. C., Kazantzidis S., Weinberg D. H., Guedes J., Callegari S., Mayer L., Madau P., 2013, ApJ, 773, 43

Bird J. C., Loebman S. R., Weinberg D. H., Brooks A. M., Quinn T. R., Christensen C. R., 2021, MNRAS, 503, 1815

Blitz L., Rosolowsky E., 2006, ApJ, 650, 933

Bovy J., Rix H.-W., Liu C., Hogg D. W., Beers T. C., Lee Y. S., 2012, ApJ, 753, 148

Bovy J., Rix H.-W., Schlafly E. F., Nidever D. L., Holtzman J. A., Shetrone M., Beers T. C., 2016, ApJ, 823, 30

Brunetti M., Chiappini C., Pfenniger D., 2011, A&A, 534, A75

Casagrande L., Schönrich R., Asplund M., Cassisi S., Ramírez I., Meléndez J., Bensby T., Feltzing S., 2011, A&A, 530, A138

Cautun M., et al., 2020, MNRAS, 494, 4291

Chiappini C., Matteucci F., Gratton R., 1997, ApJ, 477, 765

Ciucă I., Kawata D., Lin J., Casagrande L., Seabroke G., Cropper M., 2018, MNRAS, 475, 1203

Colless M., et al., 2003, arXiv e-prints, pp astro–ph/0306581

Crain R. A., et al., 2015, MNRAS, 450, 1937

Dalla Vecchia C., Schaye J., 2012, MNRAS, 426, 140

Davis M., Efstathiou G., Frenk C. S., White S. D. M., 1985, ApJ, 292, 371

De Silva G. M., et al., 2015, MNRAS, 449, 2604

Deng L.-C., et al., 2012, Research in Astronomy and Astrophysics, 12, 735

Edvardsson B., Andersen J., Gustafsson B., Lambert D. L., Nissen P. E., Tomkin J., 1993, A&A, 275, 101

Fall S. M., Efstathiou G., 1980, MNRAS, 193, 189

Fattahi A., et al., 2016, MNRAS, 457, 844

Ferrero I., et al., 2017, MNRAS, 464, 4736

Frankel N., Rix H.-W., Ting Y.-S., Ness M., Hogg D. W., 2018, ApJ, 865, 96

Gaia Collaboration et al., 2018, A&A, 616, A1

Gilmore G., et al., 2012, The Messenger, 147, 25

Grand R. J. J., Kawata D., Cropper M., 2015, MNRAS, 447, 4018

Grand R. J. J., et al., 2017, MNRAS, 467, 179

Hayden M. R., et al., 2014, AJ, 147, 116

Hayden M. R., et al., 2015, ApJ, 808, 132

Haywood M., Di Matteo P., Lehnert M. D., Katz D., Gómez A., 2013, A&A, 560, A109

Helmi A., Babusiaux C., Koppelman H. H., Massari D., Veljanoski J., Brown A. G. A., 2018, Nature, 563, 85

Holmberg J., Nordström B., Andersen J., 2007, A&A, 475, 519

Hopkins P. F., 2013, Pressure-Entropy SPH: Pressure-entropy smooth-particle hydrodynamics (ascl:1305.006)

Hopkins P. F., Kereš D., Oñorbe J., Faucher-Giguère C.-A., Quataert E., Murray N., Bullock J. S., 2014, MNRAS, 445, 581

Huchra J., et al., 2005, in Fairall A. P., Woudt P. A., eds, Astronomical Society of the Pacific Conference Series Vol. 329, Nearby Large-Scale Structures and the Zone of Avoidance. p. 135

Jenkins A., Binney J., 1990, MNRAS, 245, 305

Just A., Jahreiß H., 2010, MNRAS, 402, 461

Katz N., 1992, ApJ, 391, 502

Kawata D., Grand R. J. J., Gibson B. K., Casagrande L., Hunt J. A. S., Brook C. B., 2017, MNRAS, 464, 702

Kennicutt Robert C. J., 1998, ApJ, 498, 541

Komatsu E., et al., 2011, Astrophysical Journal, Supplement, 192, 18

Kowalski M., et al., 2008, ApJ, 686, 749

Kubryk M., Prantzos N., Athanassoula E., 2015, A&A, 580, A126

Lacey C. G., 1984, MNRAS, 208, 687

Loebman S. R., Debattista V. P., Nidever D. L., Hayden M. R., Holtzman J. A., Clarke A. J., Roškar R., Valluri M., 2016, ApJ, 818, L6

Mackereth J. T., et al., 2017, MNRAS, 471, 3057

Mackereth J. T., et al., 2019, MNRAS, 489, 176

Massey R., et al., 2007, Astrophysical Journal, Supplement, 172, 239

McMillan P. J., 2017, MNRAS, 465, 76

Minchev I., 2016, Astronomische Nachrichten, 337, 703

Minchev I., Famaey B., 2010, ApJ, 722, 112

Mo H. J., Mao S., White S. D. M., 1998, MNRAS, 295, 319

Monaghan J. J., 1992, ARA&A, 30, 543

Navarro J. F., Frenk C. S., White S. D. M., 1997, ApJ, 490, 493

Navarro J. F., et al., 2018, MNRAS, 476, 3648

Pinsonneault M. H., et al., 2018, Astrophysical Journal, Supplement, 239, 32

Przybilla N., Nieva M.-F., Butler K., 2008, ApJ, 688, L103

Sales L. V., Navarro J. F., Schaye J., Dalla Vecchia C., Springel V., Booth C. M., 2010, MNRAS, 409, 1541

Sanders J. L., Das P., 2018, MNRAS, 481, 4093

Sawala T., et al., 2016, MNRAS, 457, 1931

Scannapieco C., et al., 2012, MNRAS, 423, 1726

Schaye J., et al., 2015, MNRAS, 446, 521

Schlesinger K. J., et al., 2014, ApJ, 791, 112

Schönrich R., Binney J., 2009, MNRAS, 396, 203

Sellwood J. A., Binney J. J., 2002, MNRAS, 336, 785

Snaith O., Haywood M., Di Matteo P., Lehnert M. D., Combes F., Katz D., Gómez A., 2015, A&A, 578, A87

Somerville R. S., Davé R., 2015, ARA&A, 53, 51

Springel V., 2005, MNRAS, 364, 1105

Springel V., 2010a, ARA&A, 48, 391

Springel V., 2010b, MNRAS, 401, 791

Springel V., White S. D. M., Tormen G., Kauffmann G., 2001, MNRAS, 328, 726

Springel V., Frenk C. S., White S. D. M., 2006, Nature, 440, 1137

Steinmetz M., Navarro J. F., 2002, New Astronomy, 7, 155

Steinmetz M., et al., 2006, AJ, 132, 1645

Strateva I., et al., 2001, AJ, 122, 1861

Suyu S. H., Marshall P. J., Auger M. W., Hilbert S., Blandford R. D., Koopmans L. V. E., Fassnacht C. D., Treu T., 2010, ApJ, 711, 201

Tegmark M., et al., 2004, ApJ, 606, 702

Tegmark M., et al., 2006, Physical Review D, 74, 123507

Ting Y.-S., Rix H.-W., 2018, arXiv e-prints,

Toyouchi D., Chiba M., 2018, ApJ, 855, 104

Trayford J. W., et al., 2017, MNRAS, 470, 771

Vera-Ciro C., D'Onghia E., Navarro J., Abadi M., 2014, ApJ, 794, 173

Vera-Ciro C., D'Onghia E., Navarro J. F., 2016, ApJ, 833, 42

Vikhlinin A., et al., 2009, ApJ, 692, 1060

Villalobos Á., Helmi A., 2008, MNRAS, 391, 1806

Vogelsberger M., et al., 2014, MNRAS, 444, 1518

Wadsley J. W., Stadel J., Quinn T., 2004, New Astronomy, 9, 137

Wang L., Dutton A. A., Stinson G. S., Macciò A. V., Penzo C., Kang X., Keller B. W., Wadsley J., 2015, MNRAS, 454, 83

White S. D. M., Frenk C. S., 1991, ApJ, 379, 52

White S. D. M., Rees M. J., 1978, MNRAS, 183, 341

Yanny B., et al., 2009, AJ, 137, 4377